OPEN ACCESS



X-Ray and Optical Polarization Aligned with the Radio Jet Ejecta in GX 339-4

G. Mastroserio , B. De Marco , M. C. Baglio , F. Carotenuto , S. Fabiani , T. D. Russell , F. Capitanio , F. Capitanio Y. Cavecchi², S. Motta³, D. M. Russell⁸, M. Dovčiak⁹, M. Del Santo⁷, K. Alabarta⁸, A. Ambrifi^{10,11}, S. Campana³, P. Casella⁵, S. Covino³, G. Illiano^{5,12,13}, E. Kara¹⁴, E. V. Lai¹⁵, G. Lodato¹, A. Manca¹⁶, I. Mariani³, A. Marino^{17,18}, C. Miceli^{7,19,20}, P. Saikia⁸, A. W. Shaw²¹, J. Svoboda⁹, F. M. Vincentelli²², and J. Wang¹⁴ Dipartimento di Fisica, Università degli Studi di Milano, Via Celoria 16, I-20133 Milano, Italy; guglielmo.mastroserio@gmail.com Departament de Fisíca, EEBE, Universitat Politècnica de Catalunya, Av. Eduard Maristany 16, 08019 Barcelona, Spain Istituto Nazionale di Astrofisica, Osservatorio Astronomico di Brera, via E. Bianchi 46, 23807 Merate (LC), Italy

Astrophysics, Department of Physics, University of Oxford, Keble Road, Oxford OX1 3RH, UK ⁵ INAF-Osservatorio Astronomico di Roma, Via Frascati 33, I-00076, Monte Porzio Catone (RM), Italy

⁶ INAF-IAPS via del Fosso del Cavaliere, 100, 00133 Rome, Italy ⁷ INAF, Istituto di Astrofisica Spaziale e Fisica Cosmica, Via U. La Malfa 153, I-90146 Palermo, Italy ⁸ Center for Astrophysics and Space Science (CASS), New York University Abu Dhabi, PO Box 129188, Abu Dhabi, UAE Astronomical Institute of the Czech Academy of Sciences, Boční II 1401, 14100 Praha 4, Czech Republic ¹⁰ Instituto de Astrofísica de Canarias, E-38205 La Laguna, Tenerife, Spain 11 Departamento de Astrofísica, Universidad de La Laguna, E-38206 La Laguna, Tenerife, Spain Tor Vergata University of Rome, Via della Ricerca Scientifica 1, I-00133 Roma, Italy Sapienza Università di Roma, Piazzale Aldo Moro 5, I-00185 Rome, Italy ¹⁴ MIT Kavli Institute for Astrophysics and Space Research, Massachusetts Institute of Technology, Cambridge, MA 02139, USA INAF-Osservatorio Astronomico di Cagliari, via della Scienza 5, I-09047, Selargius (CA), Italy Dipartimento di Fisica, Università degli Studi di Cagliari, SP Monserrato-Sestu, KM 0.7, Monserrato, 09042, Italy 17 Institute of Space Sciences (ICE, CSIC), Campus UAB, Carrer de Can Magrans s/n, 08193, Barcelona, Spain 18 Institut d'Estudis Espaciale de Catalunya (IEEC) 08860 Castelldefels (Barcelona) Spain ⁸ Institut d'Estudis Espacials de Catalunya (IEEC), 08860 Castelldefels (Barcelona), Spain ¹⁹ Dipartimento di Scienze Fisiche ed Astronomiche, Università di Palermo, via Archirafi 36, 90123 Palermo, Italy ²⁰ IRAP, Universitè de Toulouse, CNRS, UPS, CNES, 9, avenue du Colonel Roche BP 44346 F-31028 Toulouse, Cedex 4, France
²¹ Department of Physics & Astronomy, Butler University, 4600 Sunset Avenue, Indianapolis, IN 46208, USA Department of Physics and Astronomy, University of Southampton, SO17 1BJ, UK Received 2024 August 09; revised 2024 November 15; accepted 2024 November 28; published 2025 January 3

Abstract

We present the first X-ray polarization measurements of GX 339–4. IXPE observed this source twice during its 2023–2024 outburst, once in the soft-intermediate state and again during a soft state. The observation taken during the intermediate state shows a significant (4σ) polarization degree $P_{\rm X}=1.3\%\pm0.3\%$ and polarization angle $\theta_{\rm X}=-74^{\circ}\pm7^{\circ}$ only in the 3–8 keV band. FORS2 at the Very Large Telescope observed the source simultaneously, detecting optical polarization in the B, V, R, and I bands (between \sim 0.1% and \sim 0.7%), all roughly aligned with the X-ray polarization. We also detect a discrete jet knot from radio observations with the Australia Telescope Compact Array taken later in time; this knot would have been ejected from the system around the same time as the hard-to-soft X-ray state transition, and a bright radio flare occurred \sim 3 months earlier. The proper motion of the jet knot provides a direct measurement of the jet orientation angle on the plane of the sky at the time of the ejection. We find that both the X-ray and optical polarization angles are aligned with the direction of the ballistic jet.

Unified Astronomy Thesaurus concepts: Accretion (14); Low-mass x-ray binary stars (939); X-ray astronomy (1810); Radio astronomy (1338); Astrophysical black holes (98)

1. Introduction

Black hole X-ray binaries (BHXBs) are binary systems where a stellar-mass black hole accretes matter from a companion star. In the subclass of these objects that hosts a low-mass companion star ($M < 3 M_{\odot}$; N. E. White et al. 1995), known as low-mass X-ray binaries (LMXBs), material is transferred from the star to the black hole via Roche-lobe overflow, forming an accretion disk around the black hole. The quasi-totality of these systems is X-ray transient; i.e., they alternate monthslong X-ray-bright outbursts with longer quiescence periods when they are either not detected or very X-ray faint (B. E. Tetarenko et al. 2016). During the outburst

Original content from this work may be used under the terms of the Creative Commons Attribution 4.0 licence. Any further distribution of this work must maintain attribution to the author(s) and the title of the work, journal citation and DOI.

phase, the X-ray radiation mainly consists of a multicolor diskblackbody component from the geometrically thin, optically thick accretion disk (I. D. Novikov & K. S. Thorne 1973; N. I. Shakura & R. A. Sunyaev 1973) and a Comptonization component that is due to disk photons being upscattered by hot electrons confined in a plasma region close to the black hole, known as the "corona" (K. S. Thorne & R. H. Price 1975; C. Done & A. Kubota 2007). A portion of the latter emission is reprocessed by the disk emitting a so-called reflection component (A. C. Fabian et al. 1989). During their outbursts, the majority of these systems follow a characteristic evolution through three main states defined by the X-ray luminosity and the hardness ratio of the energy spectrum (e.g., T. M. Belloni 2010). From the quiescence phase, they enter the hard state, increasing their X-ray luminosity with a relatively hard X-ray spectrum, dominated by the coronal emission. As the outburst progresses, the energy spectrum becomes softer (over timescales of days; C. Done & A. Kubota 2007) and the X-ray luminosity slightly increases as the source enters an intermediate state. During this *intermediate state*, both the disk and coronal emissions contribute significantly to the spectrum. However, based on both the X-ray spectral and timing properties (e.g., T. Belloni et al. 2005), this state can be further subclassified into a hard-intermediate state (HIMS) and a soft-intermediate state (SIMS). The source continues to soften, transitioning toward a soft X-ray state. Once the source is in the *soft state*, it begins to slowly decay in X-ray brightness while the shape of its spectrum remains relatively constant, dominated by the disk component. Finally, the source transitions back to the hard state, tracing a hysteresis pattern in the hardness intensity diagram (HID; J. Homan et al. 2001).

The timing properties of the X-ray emission change during the outburst. The source increases its rms X-ray variability as the source brightens during the hard state, reaching a maximum at the beginning of the hard-to-soft transition (T. Muñoz-Darias et al. 2011). The variability decreases slightly during the transition, dropping to just a few percents rms during the soft state. Some of the most intriguing features are the X-ray quasiperiodic oscillations (QPOs) that appear in the hard and intermediate states. These QPOs have a characteristic frequency of $\sim 0.01-0.1$ Hz during the hard state, which moves to a few Hz during the intermediate state. QPOs are divided into three classes (P. Casella et al. 2005): type C QPOs, which are detected in all states characterized by a high amplitude (up to 20% rms); type B QPOs, which are detected only in the SIMS and usually just before the transition to the soft state with rms up to 5%; and type A QPOs, which are weaker and observed much more rarely (see A. R. Ingram & S. E. Motta 2019 for a review).

During their outbursts, BHXBs launch two types of jets, both observed in the radio band: a steady, compact jet is observed in the hard X-ray state, and a short-lived, transient jet arises during the hard-to-soft transition (e.g., R. P. Fender et al. 2004). The transient jet is composed of discrete knots of synchrotron-emitting plasma that are launched out from the system. These ejecta produce bright radio flares as they propagate outward along the jet axis (at the time of launch; J. C. A. Miller-Jones et al. 2019) at speeds that can approach the speed of light (e.g., I. F. Mirabel & L. F. Rodrìguez 1994; S. J. Tingay et al. 1995; T. D. Russell et al. 2019; J. S. Bright et al. 2020; F. Carotenuto et al. 2021).

The two main components of the X-ray emission (disk and corona) are expected to be polarized with a linear polarization fraction (P) highly dependent on the viewing angle. The radiation emerging from an extended, nonspherical region dominated by a multi-upscattering inverse Compton process is expected to show a net polarization angle (θ) parallel to the direction along which the emitting region is least extended, corresponding to its minor axis (J. Poutanen & R. Svensson 1996; J. D. Schnittman & J. H. Krolik 2010). The thermal emission from the thin accretion disk is expected to be polarized perpendicular to the plane of the disk (S. Chandrasekhar 1960; V. V. Sobolev & I. N. Minin 1963; M. Dovčiak et al. 2008; J. D. Schnittman & J. H. Krolik 2009). The recently launched Imaging X-ray Polarimetry Explorer (IXPE; M. C. Weisskopf et al. 2022) has detected significant polarization in several BHXBs. Cyg X-1 was the first black hole that showed a significant X-ray polarization measured by IXPE (H. Krawczynski et al. 2022). That system was observed during a hard state, where a 4% X-ray $P(P_X)$ was measured, with an X-ray θ (θ _X) aligned with the jet axis. Such an alignment constrains the geometry of the corona to be horizontally extended in the plane of the disk (but see also M. A. Moscibrodzka & A. I. Yfantis 2023; J. Dexter & M. C. Begelman 2024 for alternative explanations). Cyg X-1 was also observed in a soft X-ray state, and its P_X decreased to ${\sim}2\%$ compared to the hard state while $\theta_{\rm X}$ stayed constant (J. F. Steiner et al. 2024). IXPE has also observed a few transient BHXBs. Swift J1727.8–1613 was observed recently between its hard state and HIMS (A. Veledina et al. 2023). During the transition to the soft state, the P_X slightly decreased from ${\sim}4\%$ to ${\sim}3\%$ while the $\theta_{\rm X}$ stayed constant (A. Ingram et al. 2024). Importantly, the θ_X was aligned with the jet direction (C. M. Wood et al. 2024) in the soft state. LMC X-1 (J. Podgorný et al. 2023), 4U 1957+115 (L. Marra et al. 2024), LMC X-3 (J. Svoboda et al. 2024), and 4U 1630-47 (N. Rodriguez Cavero et al. 2023; A. Ratheesh et al. 2024) were observed in the soft state and all exhibit significant P_X ranging from $\sim 1\%$ up to \sim 8%. While the sources with relatively low $P_{\rm X}$ (<3%) are easier to explain, reconciling the high $P_{\rm X}$ (up to \sim 8%) and the alignment of the θ_X of the thermal and nonthermal components of 4U 1630-47 with theoretical models is more complicated considering the not-extremely-high source inclination. These results would require an outflowing disk atmosphere and returning radiation from the accretion disk (J. D. Schnittman & J. H. Krolik 2009; R. Taverna et al. 2021) to explain the high $P_{\rm X}$ and the alignment of the different components' $\theta_{\rm X}$, respectively (A. Ratheesh et al. 2024 and references therein).

1.1. GX 339-4 2023-2024 Outburst

GX 339–4 is an LMXB discovered in 1972 (T. H. Markert et al. 1973). The source goes into full outburst²³ every 2–3 yr, although there does not appear to be any specific periodicity (K. Alabarta et al. 2021), moving through all of the X-ray states (e.g., D. S. Plant et al. 2014). For these reasons, GX 339–4 is often considered the archetypal LMXB, often used to explain typical source behaviors and as a comparison source. Despite many outbursts, the distance, inclination, and mass of GX 339–4 have not been precisely determined. A. A. Zdziarski et al. (2019) recently revised some of these parameters, claiming a narrower range for the inclination of \sim 40°–60° (compared to the \sim 37°–78° of M. Heida et al. 2017), resulting in a distance to the source of \sim 8–12 kpc and a mass between 4 and 11 M_{\odot} (which is slightly higher than the previous constraint of 2.3–9.5 M_{\odot} ; M. Heida et al. 2017).

GX 339–4 started its most recent outburst in 2023. From 2023 mid-August, the Las Cumbres Observatory detected an increase in the source's optical flux (K. Alabarta et al. 2023). In 2023 October, the Monitor of All-sky X-ray Image (MAXI) measured an X-ray flux of 0.033 ± 0.007 photons cm⁻² s⁻¹ in the 2–10 keV energy band (H. Negoro et al. 2023), while MeerKAT detected the initial brightening of the radio jet (M. M. Nyamai et al. 2024). On 2024 January 25, GX 339–4 began a hard-to-soft transition (H. Negoro et al. 2024; M. M. Nyamai et al. 2024), which was then followed by a fading phase in the optical (K. Alabarta et al. 2024). In Appendix A, we compare the 2023–2024 outburst with the last four outbursts of GX 339–4. In this Letter, we analyze two

²³ LMXBs, including GX 339–4, may also go through "failed" outbursts, where the source does not transit through all of the states, often remaining in a hard state only (B. E. Tetarenko et al. 2016).

IXPE observations performed during the 2023–2024 outburst in the SIMS and in the soft state. Thanks to simultaneous observations with other X-ray telescopes (Swift/X-Ray Telescope, Neutron Star Interior Composition Explorer (NICER), and Nuclear Spectroscopic Telescope Array (NuSTAR)), we were able to constrain the spectral-timing-polarimetric properties of the source. With the optical (FORS2 at the Very Large Telescope, VLT) and radio (Australia Telescope Compact Array, ATCA) coverage, we measured the optical polarization and the orientation of the radio jet.

2. The Multiwavelength Campaign

2.1. X-Ray Data

All the X-ray observations have been reduced using the HEAsoft²⁴ release 6.33.

IXPE. IXPE observed the source twice, once during the SIMS state and once during the soft state (see Table 2 in Appendix A for the details). Hereafter, we will refer to these observations as epoch 1 and epoch 2. For both observations, we extracted the source region using the SAOImageDS9²⁵ software. We used a 60" circle centered at the peak of the source counts for each IXPE detector. We applied the NEFFweighting analysis (L. Baldini et al. 2022; A. Di Marco et al. 2022) extracting the energy spectra of the Stokes parameters I, Q, and U using XSELECT from HEAsoft. Finally, we produced the detector Modulation Response File and Ancillary Response File responses using the ftool ixpecalcarf, and we used ixpe_d2_20170101_alpha075_02.rmf as the detector Response Matrix File. In both epoch 1 and epoch 2, we neglected the background contribution since the source is sufficiently bright (see A. Di Marco et al. 2023 for a complete explanation of the background subtraction in IXPE). The spectra were not rebinned during the fit, although they have been rebinned for visual purposes only in this Letter.

Swift/X-Ray Telescope (XRT). Swift/XRT (D. N. Burrows et al. 2005) observed GX 339-4 during the IXPE observations multiple times in Window Timing (WT) mode (see Table 2 for details). The Swift/XRT data were reprocessed with the task xrtpipeline, included in the HEAsoft package, and the employed CALDB files were released on July 25, 2023 (20230725). Events with grades 0 were selected to reduce the effect of energy redistribution at low energies that is known to affect XRT data for bright, heavily absorbed sources. ²⁶ Since the count rate in WT mode was higher than 100 counts s⁻¹, we applied the pileup correction procedure by filtering the event files using an annulus region centered on the source position with an inner radius of 6 pixels (the outer radius was 20 pixels). The same annulus positioned at the end of the stripe (on the WT image) was used for the background extraction. Then both the source and background spectra were extracted running the task xrtproducts. We found instrumental features in the spectra near the gold edge (2.2 keV) and the silicon edge (1.84 keV), which are usually seen in high signal-to-noise WT spectra²⁷ and are taken into consideration during the fitting procedure.

NICER. NICER (J. Gendreau et al. 2016) monitored GX 339-4 during the 2023-2024 outburst. The observations considered in this Letter started on 2024 January 31 (see Table 2 for the details). The X-ray Timing Instrument observations were reduced using the NICER pipeline NICER-DAS distributed with HEAsoft, the calibration file released on February 6, 2024 (20240206), and updated geomagnetic data. Calibration and screening of the data were performed using the nicer12 task, limiting the undershoot rate to ≤ 200 counts s⁻¹ and the overshoot rate to ≤ 1 count s⁻¹. Focal plane modules (FPMs) 14 and 34 were filtered out due to occasional increased detector noise. We extracted light curves using the task nicer13-1c. All NICER spectra were produced using the nicerl3-spect task, adopting the NICER SCORPEON background model. We note that all NICER data of epoch 2 were taken during orbit day; thus, all the results are severely affected by the optical light leak that NICER has been experiencing since 2023 May 22. We verified that the undershoot rate always exceeds 600 counts s⁻¹ in this epoch. For this reason, we could not use these data for the analysis. For self-consistency, after checking against the NICER spectra of epoch 1, we decided to fit the energy spectra using only Swift/XRT for both epochs and to use the NICER data just for the timing analysis.

NuSTAR. NuSTAR (F. A. Harrison et al. 2013) observed the source during both epoch 1 and epoch 2 (see Table 2 for the details). The same reduction procedure was applied to both observations. We used the nupipeline²⁸ routine distributed from HEAsoft to produce the event files and with the calibration files released on March 25, 2024 (20240325). The extraction region was a circle of 80" centered on the source for both epochs. We ran nuproducts to produce the energy spectra and ftgrouppha to rebin them with grouptype=optmin, which uses the J. S. Kaastra & J. A. M. Bleeker (2016) optimal rebinning with the minimum counts per bin set to 30. The NuSTAR background was extracted from a field-of-view region of 80" without including the source. Since the source is bright, we could not choose this region in the same detector of the source.

2.2. Optical Observations

GX 339-4 was observed with the FORS2 mounted on the VLT (Cerro Paranal, Chile) on 2024 February 15, March 2, and March 16. The first observation is simultaneous with IXPE epoch 1, whereas the other two are close to epoch 2 (see Table 2 for the details). A Wollaston prism was placed in the instrument's light path, dividing the incoming radiation into two orthogonally polarized light beams (ordinary and extraordinary). A Wollaston mask prevented these beams from overlapping on the CCD. Additionally, a rotating half-wave plate (HWP) was installed, enabling images to be captured at four different angles (Φ_i) relative to the telescope axis: $\Phi_i = 22^{\circ}.5(i-1), i = 1, 2, 3, 4$. This step is crucial for obtaining a polarization measurement, as the images taken at >two different angles must be combined to determine the level of linear polarization, as described in Appendix A.2. Four sets of images were taken with this configuration, one for each available optical band (I_BESS+77, R_SPECIAL+76, v_HIGH +114, and $b_HIGH+113$, hereafter I, R, V, and B), with exposure times of 20 s, 15 s, 10 s, and 25 s for each image in

²⁴ https://heasarc.gsfc.nasa.gov/docs/software/heasoft/

www.sites.google.com/cfa.harvard.edu/saoimageds9

²⁶ See http://www.swift.ac.uk/analysis/xrt/digest_cal.php for details.

http://heasarc.gsfc.nasa.gov/docs/heasarc/caldb/swift/docs/xrt/SWIFT-XRT-CALDB-09_v19.pdf

 $[\]overline{^{28}}$ Adding the specific statusexpr="STATUS==b0000xxx00xxxx000".

 Table 1

 Results of the VLT/FORS2 (BVRI Filters) Polarimetric Campaign

Date	В		V		R		I	
	P (%)	θ (deg)	P (%)	θ (deg)	P (%)	θ (deg)	P (%)	θ (deg)
2024 Feb 15	$0.65^{+0.14}_{-0.15}$	129 ± 6	0.35 ± 0.10	124 ± 8	$0.67^{+0.08}_{-0.09}$	128 ± 3	0.17 ± 0.05	103 ± 8
2024 Mar 02	2.1 ± 0.2	87 ± 3	0.4 ± 0.1	180 ± 8	$0.76^{+0.08}_{-0.09}$	119 ± 3	0.24 ± 0.05	148 ± 5
2024 Mar 16	0.5 ± 0.1	96 ± 7	$0.26^{+0.07}_{-0.08}$	139^{+7}_{-8}	$0.17^{+0.05}_{-0.06}$	124^{+9}_{-10}	<0.21%	88 ± 15

Note. All the polarization levels and angles are corrected for instrumental polarization. The interstellar polarization has also been subtracted by means of a group of reference stars in the field. Upper limits are indicated at a 99.97% confidence level and the rest of the errors at 1σ confidence.

the four different filters, respectively. Two more sets of observations were then acquired with the same configuration on different dates: 2024 March 2 and March 16. These two observations bracket—and are intended to be almost simultaneous with—the IXPE epoch 2 (2024 March 8–10). All three observations were performed under photometric conditions, with seeing in the range of 0."3–0."4. All images were processed by subtracting an average bias frame and dividing by a normalized flat field (see additional details of the analysis in Appendix A.2). We report the results of our optical polarization analysis in Table 1.

2.3. Radio Observations

We observed GX 339–4 with ATCA on 2024 May 1 between 16:30 UT and 23:13 UT (under program C3362; PI: Carotenuto). ATCA was in its most extended 6A configuration. Data were recorded simultaneously at central frequencies of 5.5 GHz and 9.0 GHz, with 2 GHz of bandwidth at each frequency. We used PKS B1934–638 for bandpass and flux density calibration, and B1646–50 for the complex gain calibration. Data were flagged, calibrated, and imaged using standard procedures within the Common Astronomy Software Applications for radio astronomy (version 5.1.2; CASA²⁹ Team et al. 2022). When imaging, we used a Briggs robust parameter of 0 to balance sensitivity and resolution (S. D. Briggs 1995).

3. HID and Source Evolution

During the beginning of 2024, GX 339-4 NICER visibility was Sun-constrained; thus, the observatory could not perform its typical daily observational campaign. However, MAXI (M. Matsuoka et al. 2009) and Swift/Burst Alert Telescope (BAT; S. D. Barthelmy et al. 2005) were able to observe the source almost every day, and we could follow the evolution of the spectral hardness during the outburst. Figure 1 shows the HID of the 2023-2024 outburst. The time evolution of the source is indicated by the different colors of the data points. The top right inset shows a zoom of NICER observations (from ObsID 7702010107 to ObsID 7702010118). The two IXPE observations of the source are indicated with the magenta symbols. The second IXPE observation was performed on the same day as a MAXI pointing; thus, we could easily place this observation on the HID. Unfortunately, the first IXPE observation was performed during a gap in the MAXI monitoring. We used the NICER data to track the evolution of the source during this period. The spectral hardness of the NICER data was computed using the same energy ranges used for MAXI (4-10 keV and 2-4 keV). However, the two

instruments have different effective areas, and both hardness and count rates are not trivial to compare. We decided to "calibrate" the NICER count rates and hardness to match the MAXI values. We assigned to the NICER ObsID 7702010107 starting at MJD 60350.2924 (first point on the left in the inset of Figure 1), the same count rate and hardness values as the MAXI observation at MJD 60350.5. This is the last MAXI observation before the MAXI gap; thus, we start using the NICER data from here. We then applied a correction factor to the NICER data to match the relative variations of hardness and rates observed in MAXI.

As has often been observed in the past (e.g., T. Belloni et al. 2005), GX 339–4 did not smoothly transition to the soft state but went through a number of back-and-forth transitions across the SIMS. We start to observe this behavior during the MAXI gap. Past outbursts showed that, during this "hesitation" period, it is common to observe type B QPOs appearing and disappearing in the power density spectrum (PDS; S. Motta et al. 2011).

4. Fast X-Ray Variability and Type B QPOs

We analyzed the fast X-ray variability of GX 339–4 using NICER and NuSTAR data in order to better characterize the accretion state of the source and look for the presence of QPOs. For the NICER data, we used 2–10 keV light curves with a time bin of 0.0004 s and extracted a PDS for each observation using segments of 40 s length. For the NuSTAR data, we used 3–80 keV light curves with a time bin of 0.001 s and extracted the PDS using segments of 100 s length. We used the stingray software (D. Huppenkothen et al. 2019; M. Bachetti et al. 2024) to generate the PDS and the Fourier amplitude difference to correct for dead time (M. Bachetti & D. Huppenkothen 2018). A small time bin allowed us to obtain a good sampling of the Poisson noise contribution to the PDS, which we fitted at frequencies >100 Hz with a constant model and subtracted out.

A strong type B QPO on top of a weak red noise continuum is detected in the NuSTAR and NICER observations simultaneous to IXPE epoch 1. In Figure 2, we show the PDS obtained by combining the three NICER observations simultaneous to epoch 1 (see Figure 6). Overplotted are the NuSTAR PDSs simultaneous to epochs 1 and 2. A logarithmic rebinning was applied to all the PDSs. More specifically, the QPO is observed in each of the three NICER observations simultaneous to epoch 1, as well as in each of the NuSTAR orbits, suggesting that the source variability does not change significantly during epoch 1. On the other hand, epoch 2 does not show significant fast variability during the NuSTAR observation (see gray PDS in Figure 2). The intensive NICER monitoring shows that the type B QPO was not present over the 14 days preceding epoch 1, while it intermittently appeared and

²⁹ https://casa.nrao.edu

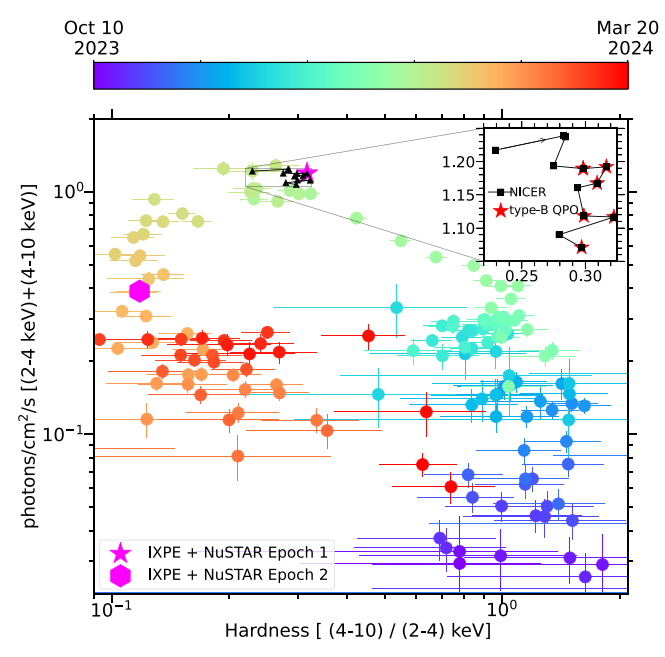


Figure 1. HID of GX 339–4 2024 outburst computed by MAXI. The color scheme indicates the time order of the observations showing that the source starts in the hard state (purple points at the bottom right) and ends with the soft-to-hard transition (red points) following a counterclockwise evolution. The black points are NICER observations (from ObsID 7702010107 to ObsID 7702010118) with spectral hardness and count rate converted to the MAXI values (see the main text for details). The inset shows the zoomed-in NICER data in the HID, and the red stars indicate the observations showing a type B QPO. Finally, the two magenta symbols represent the first (star) and second (hexagon) IXPE observations simultaneous with NuSTAR and Swift/XRT.

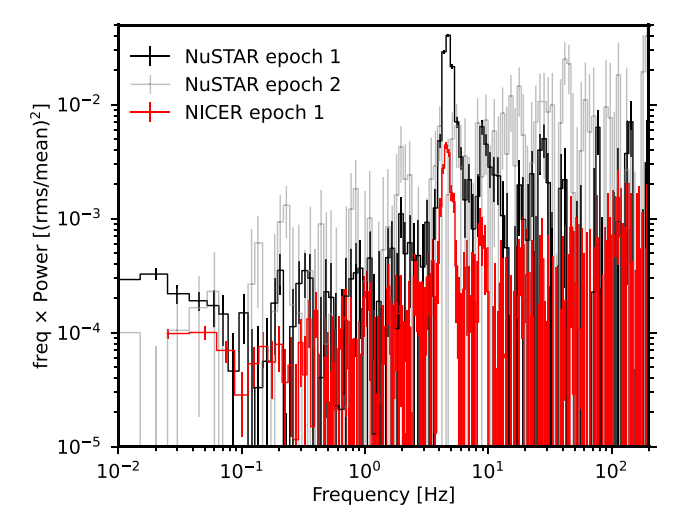


Figure 2. The Poisson noise-subtracted PDS obtained from NuSTAR (black and gray points for epochs 1 and 2, respectively) and NICER (red points) data. The NuSTAR PDS is computed from the single observations during each epoch, while the NICER PDS is computed by combining the three observations of epoch 1. The two PDSs have different powers due to the different energy ranges of the two instruments; the type B QPO is stronger in NuSTAR due to the higher energy range considered.

disappeared during the 5 days of coverage following epoch 1. As previously pointed out, this behavior had already been seen in past outbursts (E. Nespoli et al. 2003; S. Motta et al. 2011). NICER observations containing a type B QPO are marked with red stars in the inset of Figure 1. Using a Lorentzian component to model the type B QPO, we verified that its best-fit centroid frequency does not change significantly among NICER

observations. The best-fit centroid frequency of the type B QPO is $4.56 \pm 0.03\,\mathrm{Hz}$ for NICER combined data and $4.65 \pm 0.02\,\mathrm{Hz}$ for NuSTAR data. The fractional rms of the QPO is $9\% \pm 2\%$ for the NuSTAR data and $3.2\% \pm 0.2\%$ for the NICER data. Since the type B QPO rms as a function of energy increases (e.g., P. Casella et al. 2005; T. M. Belloni et al. 2020), the difference is due to the different energy bands of the two instruments.

Given these results, and following the classification proposed in T. Belloni et al. (2005), we infer that GX 339–4 was likely in a SIMS during the first IXPE observation. The lack of significant variability power in epoch 2, combined with the lower values of spectral hardness (Figure 1), suggests that the source was in a soft state during the second IXPE observation, as also confirmed by the results of our spectral analysis (Section 5.1).

Adopting the same time bin and segment length as used for extracting the PDS, we searched for soft X-ray lags between the 0.5–1 and 2–4 keV energy bands in the analyzed NICER observations of epoch 1. No clear evidence of soft lags was found due to the very low variability of the source (the measured fractional rms was only a few percent) as well as its lower flux compared to sources where these lags were previously observed. Altogether, these factors contribute to greatly reduce the sensitivity of lag measurements (e.g., P. Uttley et al. 2014).

5. Spectropolarimetric Analysis

We fitted the energy spectra of the two epochs simultaneously using IXPE, NuSTAR, and Swift/XRT data. We considered the three Swift/XRT observations during epoch 1 and the only Swift/XRT observation (ObsID 00016552003) simultaneously in epoch 2 (Table 2). We first performed the broadband spectral analysis of the two epochs using the Swift/XRT and NuSTAR data simultaneously. After constraining the best-fit spectral model, we added the IXPE data (Section 5.2) in order to constrain the $P_{\rm X}$ and $\theta_{\rm X}$ of the source. The errors on the parameter values in this section are expressed at 90% confidence if not specified otherwise.

5.1. Spectral Fit

Preliminary fits with simple models show that in both epochs, the disk and the Comptonization components contribute to the fit. Both epochs also show strong Fe K α line residuals, even though there is no evidence of residuals in the Compton hump energy range. Therefore, we decided to fit epoch 1 and epoch 2 simultaneously with the model TBnew feo * (thcomp kerrbb + relline) smedge. The kerrbb model component allows the simultaneous fit of the two epochs to be as self-consistent as possible since the only parameter free to vary between the epochs is the mass accretion rate.³¹ The thcomp model component computes the Comptonization using the seed photons of kerrbb, preventing any inconsistency between these two components.³² The choice of not including a more sophisticated reflection model (such as the relxill model; T. Dauser et al. 2014; T. Garcia et al. 2014) is dictated by the

³⁰ We used Swift/XRT instead of NICER in both epochs for consistency reasons (NICER data during epoch 2 cannot be used due to instrumental issues; see Section 2.1).

³¹ In the diskbb model, both temperature and normalization parameters are free to vary.

³² We did not use the nthcomp model because it allows the Comptonization flux to increase independently of the seed photon component's flux.

fact that such a model would overfit the Compton hump (R. M. T. Connors et al. 2021). Additionally, the adopted model allows us to easily separate the contribution of the iron line component from the polarization data (Section 5.2). Since the distance, inclination, and black hole mass of GX 339–4 are not well known, we fix the distance to 10 kpc and the mass to $10\,M_\odot$ (A. A. Zdziarski et al. 2019), and we tie the inclination between the two epochs, leaving it free to vary between $\sim 30^\circ$ and 80° (M. Heida et al. 2017). Additional details on the spectral fits are given in Appendix B.

According to our best fit of both epochs simultaneously (reduced $\chi^2 = 2461/2254$), the inclination is pegged at the lower limit $i = 30^{\circ}$. This value is slightly lower than the range of $\sim 40^{\circ} - 60^{\circ}$ reported by A. A. Zdziarski et al. (2019). The spin and the mass accretion rate are also free parameters of the fit, with the latter left free to vary between the two epochs. We note that the spin value we find ($a = 0.85 \pm 0.01$) is at risk of high degeneracy with other parameters of kerrbb. Moreover, the uncertainty we quote corresponds solely to the statistical errors and does not include any uncertainty due to model-dependent systematics. A robust estimate of the black hole spin requires thorough testing of different models, possibly combining data from more than two observing epochs. However, this is beyond the scope of this work. Here we are primarily interested in estimating the contribution of the main spectral components to the X-ray spectrum to correctly interpret the polarization results (Section 5.2). The overall unabsorbed flux decreased between the two epochs; e.g., the E = 2-10 keV flux is $F_{2-10 \text{ keV}} = (9.55 \pm 0.01) \times 10^{-9} \text{ erg cm}^{-2} \text{ s}^{-1}$ in epoch 1 and $F_{2-10 \text{ keV}} = (3.32 \pm 0.01) \times 10^{-9} \text{ erg cm}^{-2} \text{ s}^{-1}$ in epoch 2.³³ According to the results of our fit, this is driven by a significant reduction of the disk mass accretion rate, from $\dot{M} =$ $1.06^{+0.13}_{-0.04} \times 10^{18} \,\mathrm{g \, s^{-1}}$ in epoch 1 to $\dot{M} = 0.45^{+0.02}_{-0.05} \times 10^{18} \,\mathrm{g \, s^{-1}}$ in epoch 2. We also note that the covering fraction of the Comptonization model dropped from $0.17^{+0.02}_{-0.01}$ in epoch 1 to $0.029_{-0.014}^{+0.002}$ in epoch 2. This result is not surprising since the corona is expected to reduce its contribution as a source transitions to the soft state. The results of our spectral fits indicate that the spectrum is compatible with what is expected for a SIMS and a soft state during the first and second epochs, respectively. These results also agree with our conclusions from the analysis of the fast X-ray variability (Section 4).

5.2. Polarization Fit

We detected significant polarization in the 3–8 keV energy range of epoch 1, while no significant polarization (above 3σ) was detected in epoch 2.

We included the IXPE spectra in the fit, considering IXPE epoch 1 first. The parameters of the joint epoch model were fixed to their best-fit values (see Table 3), apart from the calibration constants accounting for the different normalizations of different instruments and detectors. The spectra of the Stokes parameter *I* require adding a gain shift model, which allows the fit to shift the energies on which the response matrix is defined. We report the gain values in Table 3. We verified that leaving the best-fit parameters free to vary after the addition of the IXPE spectra does not cause the parameters to change significantly.

We then fit the Stokes parameters Q and U of all three detectors considering either the full IXPE energy range ($E=2-8\,\mathrm{keV}$) or separating the IXPE band into the two subranges $E=2-3\,\mathrm{keV}$ and

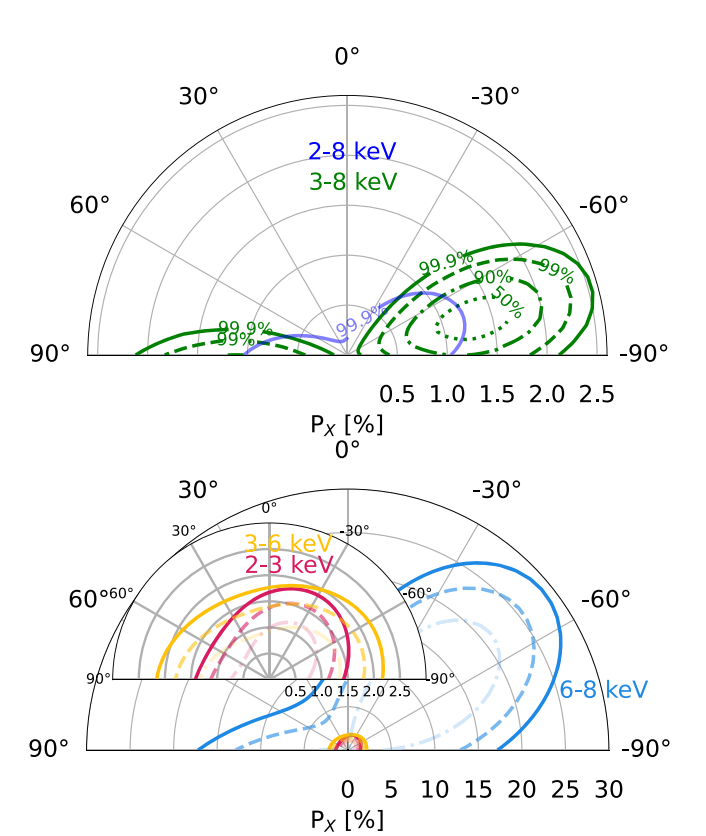


Figure 3. The epoch 1 (top panel) and epoch 2 (bottom panel) $P_{\rm X}$ and $\theta_{\rm X}$ contour levels from the simultaneous IXPE, Swift/XRT, and NuSTAR best fits (see Section 5 for details about the spectral polarimetric fit). The $P_{\rm X}$ and $\theta_{\rm X}$ calculation of epoch 1 in the IXPE 3–8 keV energy band shows significant polarization (the 99.9% contour, green solid line, closes before zero), while the full IXPE band (blue solid line, 99.9% contour) does not show any significant polarization as in all the contours in epoch 2. The inset of the bottom panel is the zoom-in of the main plot. In the bottom panel, the line styles are the same as indicated for the top panel.

E = 3-8 keV. This choice is justified by the presence of the two main components in the spectrum, the disk and the Comptonization component, with the former dominating the softer energy range and supposed to be less polarized than the latter. The polconst model was applied to our best-fit model (found before considering IXPE); thus, differences in polarization among spectral components were not accounted for at this stage (see Appendix B for additional details on the spectral polarization analysis). The top panel of Figure 3 summarizes our polarization results for epoch 1. We note that the 99.9% contour level of the IXPE full energy range does not close before the zero of P_X ; however, in the 3–8 keV energy range, we detect a significant polarization of $1.3\% \pm 0.3\%$ (1σ error). We calculated the significance with the steppar command in xspec, which shows that zero polarization is rejected with $\Delta \chi^2$ of 16.574, i.e., just above the 4σ significance. The $\theta_{\rm X}$ is also constrained to $-74^{\circ} \pm 7^{\circ}$ (1 σ error). We did not detect any significant polarization in the 2-3 keV energy range.

We followed the same procedure to perform the spectral polarization fit of the second epoch. We could not detect any significant polarization either in the full IXPE energy range or in any tested subenergy range, only an upper limit at $P_{\rm X} < 1.2\%$ (at a 3σ confidence level). We note that the most

 $[\]overline{^{33}}$ The unabsorbed flux was estimated with the model cflux in xspec.

 $[\]overline{^{34}}$ The 50% confidence level $P_{\rm X}$ contour is compatible with zero polarization.

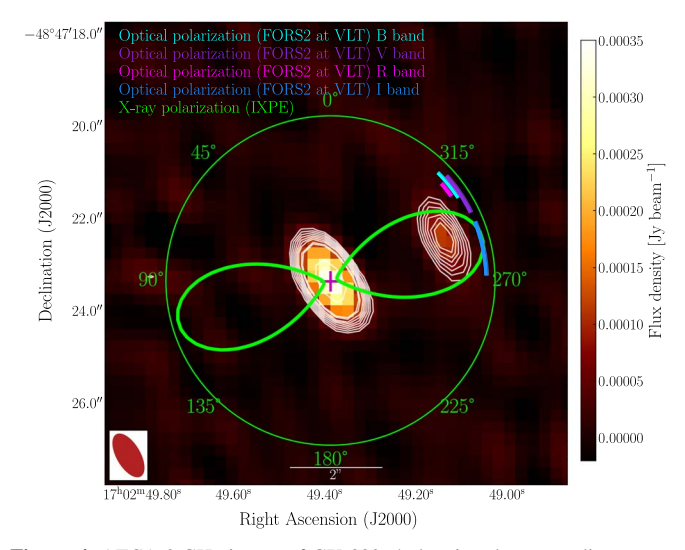


Figure 4. ATCA 9 GHz image of GX 339–4 showing the two radio sources, with the central source being associated with the core position of GX 339–4 and the NE component being the discrete knot that was ejected from the system along the jet axis at a position angle of $-69^{\circ}.54 \pm 1^{\circ}.1$ east of north. The ATCA beam, shown in red in the bottom left corner, is $1^{\circ}.5 \times 0^{\circ}.7$. The white radio contours start at 3 times the image noise rms, which is $10~\mu\mathrm{Jy}~\mathrm{beam}^{-1}$. GX 339–4's position is marked with a magenta plus sign. We also display in green the IXPE polarization 99.9% contours in 3–8 keV, which is the same solid line of Figure 3 ($P_\mathrm{X} = 1.3\% \pm 0.3\%$, $1\sigma~\mathrm{error}$). The color bands on the green circle indicate the optical polarization angle θ of the four bands that we measure in epoch 1 (the values of the optical P are reported in Table 1).

significant $P_{\rm X}$ is measured in the 6–8 keV IXPE energy range (see bottom panel of Figure 3). Only the 90% confidence level contour closes before $P_{\rm X}=0$, which cannot be considered a detection. However, it is interesting to note that the $\theta_{\rm X}$ of this contour is aligned with the $\theta_{\rm X}$ of epoch 1. All the reported results are compatible with the same energy range analysis of epoch 1 and epoch 2 performed using the IXPE pipeline <code>ixpeobssim</code>.

Finally, we fit the energy spectrum of just epoch 1 with the model TBnew (diskbb + nthcomp + relline) * smedge to be able to assign the polarization model (polconst) to each component. Although we use a different model, several parameters remain the same as in the previous model we applied to fit both epoch 1 and 2. The best-fit values of these parameters are compatible with the best fit of the previous fit (see Table 3 in Appendix B). Computing the 2D contours between the disk polarization ($P_{X,disk}$) and the coronal polarization ($P_{X,nth}$), we find that the polarization could be caused by each of the two components independently of the assumed offset between their θ_X values (i.e., either aligned or perpendicular; see Figures 8 and 9 in Appendix B).

6. Detection of a Discrete Jet Ejection

In Figure 4, we present the ATCA image at 9 GHz (having a higher resolution than the 5.5 GHz map). The image shows two components: a stronger component located at the known position of GX 339–4 and a second component located to the NW of the first at coordinates (J2000) R.A. = $17^{h}02^{m}49^{s}.139 \pm 0.000$ and

decl. = $-48^{\circ}47'23''.42 \pm 0''.04$. The angular separation between the two components is $2''.6 \pm 0''.1$.

The first component has a flux density of $400 \pm 6 \,\mu \rm Jy$ at 5.5 GHz and $356 \pm 8 \,\mu \rm Jy$ at 9 GHz, implying a radio spectral index $\alpha = -0.23 \pm 0.05$ (where the radio flux density follows $S_{\nu} \propto \nu^{\alpha}$), which is typical of the jets usually observed during the low hard state of this source (e.g., S. Corbel et al. 2013). The second component located 2.6 away has a flux density of $160 \pm 8 \,\mu \rm Jy$ at 5.5 GHz and $122 \pm 6 \,\mu \rm Jy$ at 9 GHz, indicating $\alpha = -0.6 \pm 0.1$, typical of optically thin ejecta launched from a BHXB around the hard-to-soft state transition (e.g., S. Corbel et al. 2002).

Considering the image position at the known location of GX 339-4 and its radio spectral flatness, we associate the first component with a compact jet (e.g., R. P. Fender et al. 2004) that reactivated as the source returned to the hard state during the outburst decay (T. D. Russell et al. 2024). On the other hand, the second component is the result of a discrete ejection that occurred earlier during the outburst, most likely being ejected around the hard-to-soft state transition and having propagated outward. This ejected knot remained radio-bright as it interacted with its surroundings. Using the position of the ejected component and the core emission, we determine the jet orientation angle on the plane of the sky to be $-69^{\circ}.5 \pm 1^{\circ}.1$ east of north (at the time of the ejection). This jet orientation is fully consistent with the position angle of the ejecta reported in E. Gallo et al. (2004). Given the large distance of GX 339-4 (A. A. Zdziarski et al. 2019), resolving the compact jets to determine their position angle is particularly challenging (e.g., C. M. Wood et al. 2024); as such, spatially resolving ejected jet components is crucial, as it is often the only way to infer the jet orientation angle. If the ejected component was launched at or around the start of a bright radio flare that was observed on January 31 (MJD 60340; M. M. Nyamai et al. 2024), the observed angular separation between the core and the ejection would imply a time-averaged proper motion of \sim 28.5 mas day⁻¹, which is consistent with previous findings about this source (E. Gallo et al. 2004).

7. Discussion

We present the analysis of two IXPE observations of the BHXB GX 339–4 during its 2023–2024 outburst. The first and second IXPE epochs were taken during the intermediate state and the soft state, respectively. The Swift/XRT, NICER, and NuSTAR X-ray telescopes observed the source simultaneously with IXPE during both epochs, while radio and optical observations with ATCA and VLT provided information on the multiwavelength behavior of the source.

7.1. Corona on the Disk Plane

We have measured a 1.3% \pm 0.3% (1 σ error) polarization fraction of GX 339–4 in the 3–8 keV energy band, when the source was transitioning through the SIMS during epoch 1. At the same time, type B QPOs were detected in the NICER and NuSTAR light curves. Such a feature has been proposed to be linked with the launch of relativistic jets (P. Soleri et al. 2008; R. P. Fender et al. 2009; J. C. A. Miller-Jones et al. 2012; T. D. Russell et al. 2019; J. Homan et al. 2020; D. M. Russell et al. 2020; F. Carotenuto et al. 2021; C. M. Wood et al. 2021). The connection between jets and type B QPOs is still largely debated, and no physical model to interpret it has been

 $^{^{\}overline{35}}$ We use the model <code>TBnew</code> (polconst*diskbb + polconst*nthcomp + polconst*relline) * smedge where each of the polconst has its own $P_{\rm X}$ and $\theta_{\rm X}$ parameter.

 $^{^{36}}$ $P_{\rm X}$, relline is fixed to zero (F. Podgorný et al. 2022).

conclusively identified yet. X-ray and radio observations of the black hole binary MAXI J1820+070 showed that relativistic ejections occurred nearly simultaneously with the appearance of a type B QPO (J. Homan et al. 2020). This provides the strongest empirical evidence so far for a physical link between type B QPOs and the launch of jet ejecta. Previously, this connection had only been inferred indirectly based on the viewing angle dependence of type B QPO strength: these QPOs appear stronger in nearly face-on sources, where the observed jet power is also expected to be higher (S. E. Motta et al. 2015).

Based on our results, it is reasonable to associate the jet ejection observed in the ATCA data with the radio flare detected by MeerKAT two weeks before IXPE epoch 1.

The measured direction of the jet on the plane of the sky is compatible with both the X-ray and optical polarization angles measured by IXPE and FORS2 in epoch 1, which would position the corona perpendicular to the emitted jet. In order to confirm this interpretation, we need to prove that the measured $P_{\rm X}$ is due to the coronal component. Our fit, which assigns a distinct polarization to the disk and the Comptonization, reveals that both components could be responsible for the detected polarization in GX 339-4. However, since the second IXPE epoch, which corresponds to a disk-dominated spectrum, does not show any significant polarization, we speculate that the detected polarization in epoch 1 is likely to be ascribed to the Comptonization emission. If this is the case, the corona should be horizontally extended on the plane of the accretion disk, since photons emitted after multiple scatterings are polarized perpendicular to the accretion disk and the corona itself. In this scenario, the alignment of the optical polarization with the X-ray polarization suggests that the disk plane lies on the plane defined by the binary orbit. The optical polarization would then arise from Thomson scattering in the outer accretion disk, similarly to what has been reported for A0620-00, GRO J1655-40, and Cyg X-1 (J. F. Dolan & S. Tapia 1989; M. Gliozzi et al. 1998; H. Krawczynski et al. 2022). We note that the optical polarization is very low (<1%), as typically observed for BHXBs at relatively low inclinations as GX 339-4 (J. Poutanen et al. 2018; V. Kravtsov et al. 2022). This interpretation is also supported by the decreasing trend of the optical linear polarization toward the I band (i.e., the lowest optical frequency in our data set) in all three VLT epochs (Table 1). This behavior is in fact expected since the disk is typically more dominant at the highest optical frequencies (J. C. Brown et al. 1978; J. F. Dolan 1984).

7.2. Corona Geometry in the SIMS

Our X-ray polarization analysis, combined with results from optical and radio observations, suggests the corona to be horizontally extended in the SIMS. Observations of soft X-ray reverberation lags in GX 339–4 during previous outbursts revealed the presence of short lags of a few milliseconds during the hard state (B. De Marco et al. 2015, 2017; J. Wang et al. 2020, 2022). These lags have been shown to suddenly increase by a factor of \sim 10 when the source moves to the HIMS, before its full transition to the soft state (J. Wang et al. 2022). If the increase of X-ray reverberation lag amplitude before the transition is entirely due to light travel time delays, the distance between the hard X-ray dissipation region and the disk must expand. A suggested solution is that the corona vertically extends or is partly ejected, possibly provoking shocks at large distances (B. De Marco et al. 2021; J. Wang et al. 2021, 2022).

Nonetheless, there are a few caveats that need to be considered. A long X-ray reverberation lag has not yet been observed in GX 339-4 during the SIMS (a long lag in this state has been observed only in the very bright sources MAXI J1820+070 and MAXI J1348-630; J. Wang et al. 2022). Moreover, due to visibility limitations, our campaign missed the HIMS of the 2023-2024 outburst, so we cannot directly compare our data to the results on X-ray reverberation reported by J. Wang et al. (2022) for the previous outburst of GX 339-4. Therefore, if we assume that the measured polarization is intrinsic to the corona, whatever the geometry of the corona at the beginning of the transition (HIMS), it should acquire a horizontal structure when reaching the SIMS, as inferred from X-ray polarization (but see discussion in Section 7.3). On the other hand, the requirement for a horizontally extended corona during the SIMS could be relaxed if the X-ray polarization detected in this analysis originates from the reprocessing of the disk (e.g., J. D. Schnittman & J. H. Krolik 2009; R. Taverna et al. 2021).

We note that V. Peirano et al. (2023) performed a spectral timing analysis of GX 339–4 during the SIMS in the 2021 outburst, and they invoke a two-corona structure in which a vertically extended corona explains the type B QPO variability and lags and a horizontally extended corona impacts the spectral shape. This scenario (proposed also for other sources in the SIMS; F. Garcia 2021; R. Ma et al. 2023) could reconcile the need for both a vertically structured corona to explain the X-ray reverberation lags and a horizontally extended corona required by the polarization.

It is worth noting that from their X-ray polarimetric analysis of Swift J1727.8-1613 combined with the simultaneous detection of a long soft X-ray lag in the HIMS, A. Ingram et al. (2024) propose delays other than light-crossing time to significantly contribute to the observed lags (such as thermal scattering; see G. Salvesen 2022). In this context, several theoretical solutions have been proposed in recent years. For example, P. Uttley & J. Malzac (2024) showed that, when properly accounting for mass accretion rate fluctuations starting in the accretion disk and propagating into the corona (e.g., Y. E. Lyubarskii 1997; O. Kotov et al. 2001), the observed soft X-ray lags can be reproduced without the need for extremely large (neither radially nor vertically) coronae. On the other hand, A. Veledina (2018) predicts soft lags from the interplay between two Comptonization components in a horizontally stratified corona, which would cause a pivoting power law (see also G. Mastroserio et al. 2018, 2021 for a similar mechanism). Future monitoring allowing for simultaneous X-ray timing and polarimetric analysis throughout different accretion states will allow us to better test these hypotheses.

7.3. Polarization from the Jet

Alternative scenarios have been proposed to explain the alignment of $\theta_{\rm X}$ with the direction of the jet. J. Dexter & M. C. Begelman (2024) proposed a solution in which the polarization is produced by scattering concentrated along the walls of a hollow-cone jet structure and the observer's line of sight falls inside the jet hollow cone. Since the jet cone angle is not expected to be very large, observing a source at the right orientation is relatively unlikely. So far, all the BHXBs that show significant polarization together with the detection of a ballistic jet have shown a $\theta_{\rm X}$ aligned with the jet direction. Moreover, the J. Dexter & M. C. Begelman (2024) model predicts quite a high polarization, \sim 4%, while we only detect \sim 1%.

An alternative explanation is that the observed P_X is produced by optically thin synchrotron emission from accelerated particles in the jet (e.g., D. M. Russell & T. Shahbaz 2014). Following the calculation in H. Krawczynski et al. (2022), the estimated P_X from synchrotron emission is <8% for a $\sim30^{\circ}$ inclination source (see M. Lyutikov et al. 2005 for detailed calculations). For Cyg X-1, which might have a similar inclination angle to GX 339-4, the jet contribution to the soft X-ray flux is assumed to be \lesssim 5%, resulting in an estimate of $P_{\rm X} < 0.4\%$ from the optically thin synchrotron jet. In the hard state of GX 339-4, the jet contribution could be $\sim 10\%$ or less and be produced by either the optically thin synchrotron from accelerated particles (e.g., M. A. Nowak et al. 2005; P. Gandhi et al. 2011; D. M. Russell 2023) or Compton scattering and/or synchrotron self-Compton emission from the base of the jet (e.g., S. Markoff et al. 2005; R. M. T. Connors et al. 2019). However, the optically thin synchrotron jet, seen clearly at infrared wavelengths in GX 339-4 in the hard state, fades near the start of the state transition (around the time of the transition from the hard state to the HIMS; e.g., J. Homan et al. 2005; M. Coriat et al. 2009; M. Cadolle Bel et al. 2011), well before the radio emission from the jet is quenched. The X-ray contribution of the optically thin jet is therefore likely to be low during the SIMS.

Similarly, the optical P measured during the first VLT epoch (i.e., in the SIMS; Table 1) quasi-simultaneously with IXPE is unlikely to have originated from optically thin synchrotron emission from the compact jet since this component is likely to have faded before this point along the transition. The systematic lower polarization measured in all bands in the third epoch of observations (i.e., during the soft state, when the jet is even more likely to be quenched; e.g., T. D. Russell et al. 2020) with respect to the first epoch (Table 1) could suggest a weak but significant jet contribution in the first epoch. It has been shown that the jet can produce polarized light up to a few percent in the optical, depending on the level of ordering of the magnetic field lines at the base of the jet (see, e.g., D. M. Russell et al. 2016; T. Shahbaz 2019; M. C. Baglio et al. 2020). D. M. Russell et al. (2010) demonstrated that the compact jet of GX 339-4 produced a near-infrared P of a few percent (a maximum of 2%-3%) while in the hard state, with a θ of 17° \pm 1°.6, which is perpendicular to the radio jet axis and the IXPE and VLT θ presented in this work. This result indicated that the magnetic field near the base of the jet was largely tangled in the hard state, with an average direction parallel to the jet axis.

If the optical *P* in the first epoch was due to the jet, considering the measured polarization angle, this could instead suggest that at the time of our observations, the magnetic field at the base of the jet was perpendicular to its axis, similar to what was observed, e.g., in the case of a polarization flare from the BHXB V404 Cyg during its 2015 outburst (T. Shahbaz et al. 2016). However, a more likely scenario could be optical polarization from electron scattering in the disk atmosphere (J. F. Dolan & S. Tapia 1989; M. Gliozzi et al. 1998; M. C. Baglio et al. 2016; V. Kravtsov et al. 2022). A more detailed analysis of the optical emission is needed to disentangle the different scenarios for the origin of the optical linear polarization and will be presented in a dedicated follow-up work (M. C. Baglio et al. 2024, in preparation).

8. Summary and Conclusions

We have analyzed a multiwavelength campaign of GX 339–4 during the 2023–2024 outburst performed with the Swift/XRT, NICER, NuSTAR, and IXPE X-ray telescopes; the FORS2/VLT optical spectrograph; and the ATCA radio telescope. Here we summarize the results of our spectropolarimetric timing analysis.

- 1. During the first IXPE epoch, we measured relatively soft energy spectra, which still showed some contribution from a hard nonthermal component, while the PDSs displayed a clear type B QPO at 4.56 ± 0.03 Hz for the NICER data and 4.65 ± 0.02 Hz for the NuSTAR data. The QPO indicates that the source was in the SIMS during epoch 1. During the second IXPE epoch, the energy spectra were dominated by the emission from the accretion disk, which, together with the limited fast time variability observed in the PDSs, indicates that the source had transitioned to the soft state.
- 2. We measured a significant polarization in the 3–8 keV of epoch 1, with $1.3\% \pm 0.3\%$ $P_{\rm X}$ and $-74^{\circ} \pm 7^{\circ}$ $\theta_{\rm X}$. In the whole IXPE energy band, we only found upper limits of $P_{\rm X} < 1.1\%$ in epoch 1 and <1.2% in epoch 2 (at 3σ confidence level).
- 3. We estimated the jet orientation angle on the plane of the sky to be $-69^{\circ}.5 \pm 1^{\circ}.1$, based on the detection of the radio core and a moving discrete jet ejection during our ATCA observation. The $\theta_{\rm X}$ measured in epoch 1 is aligned with the direction of the jet.
- 4. We analyzed three sets of FORS2/VLT observations. We detected significant low polarization (<1%) in four bands (I, R, V, and B) during all three observations, apart from the I band in the last observation, which has only an upper limit (see Table 1). During the first observation, simultaneous with IXPE epoch 1, the θ of all four bands is compatible with θ_X and the jet direction.

Since both the X-ray and optical polarizations are relatively low, we cannot exclude any of the physical scenarios discussed in Section 7. However, based on the alignment of X-ray and optical θ with the radio jet, we favor a system configuration with the corona horizontally extended on the plane of the accretion disk and the optical radiation produced from the outer regions of the disk.

Acknowledgments

We wish to dedicate this Letter to our beloved collaborator, mentor to several of us, and friend Tomaso Belloni, who was still with us when this campaign was first conceived.

G.M. acknowledges financial support from the European Union's Horizon Europe research and innovation program under the Marie Skłodowska-Curie grant agreement No. 101107057. M.C.B. and T.D.R. acknowledge support from the INAF-Astrofit fellowship. F.C. acknowledges support from the Royal Society through the Newton International Fellowship program (NIF/R1/211296). F.C. acknowledges support from the INAF grant 1.05.23.05.06: "Spin and Geometry in accreting X-ray binaries: The first multi-frequency spectropolarimetric campaign." Y.C. acknowledges support from the grant RYC2021-032718-I, financed by MCIN/AEI/10.13039/501100011033 and the European Union NextGenerationEU/

PRTR. B.D.M. acknowledges support via a Ramón y Cajal Fellowship (RYC2018-025950-I) and the Spanish MINECO grant PID2022-136828NB-C44. B.D.M. and Y.C. are thankful for the Spanish MINECO grant PID2020-117252GB-I00 and the AGAUR/Generalitat de Catalunya grant SGR-386/2021. E.V.L. is supported by the Italian Research Center on High Performance Computing Big Data and Quantum Computing (ICSC), project funded by European Union-NextGenerationEU—and National Recovery and Resilience Plan (NRRP)— Mission 4 Component 2 within the activities of Spoke 3 (Astrophysics and Cosmos Observations). S.F. acknowledges the support by the project PRIN 2022—2022LWPEXW—"An X-ray view of compact objects in polarized light," CUP C53D23001180006. D.M.R., P.S., and K.A. are supported by Tamkeen under the NYU Abu Dhabi Research Institute grant CASS. M.D. and J.S. thank GACR project 21-06825X for the support and institutional support from RVO:67985815. A.M. is supported by the European Research Council (ERC) under the European Union's Horizon 2020 research and innovation program (ERC Consolidator grant "MAGNESIA" No. 817661; PI: Rea). P.C. acknowledges financial support from the Italian Space Agency and National Institute for Astrophysics, ASI/INAF, under agreement ASI-INAF n.2017-14-H.O. ATCA is part of the Australia Telescope National Facility (https://ror.org/05qajvd42), which is funded by the Australian Government for operation as a National Facility managed by CSIRO. We acknowledge the Gomeroi people as the Traditional Owners of the ATCA observatory site. Part of the observations presented in this study were obtained at the European Southern Observatory under ESO program 112.25UU.001 (PI: Baglio). The authors are thankful for the team meetings at the International Space Science Institute (Bern) for fruitful discussions and were supported by the ISSI International Team project #440. M.D.S. and S.E.M. acknowledge ASI-INAF program I/004/11/6. AA acknowledges support by the Spanish Agencia estatal deinvestigación via PID2021-124879NB-I00.

Appendix A The Outburst of GX 339-4

GX 339–4 was in outburst five times in the last 15 yr (not counting the hard-only outbursts). Figure 5 shows the MAXI and Swift/BAT light curves highlighting the 2024 outburst that we consider in our work. MAXI traces the soft flux, since its energy range is 2–20 keV, and Swift/BAT observes the hard flux (15–150 keV). All the light curves are aligned at the beginning of the hard-to-soft transition, when the hard flux starts to drop in Swift/BAT. The 2024 outburst presents one of the lowest peaks of the flux among the last outbursts, especially in the soft state.

During the two IXPE epochs, GX 339–4 was observed by a few other X-ray telescopes. Figure 6 shows the light curves either simultaneous or partially simultaneous to the two IXPE observations. The IXPE and NuSTAR light curves have 50 s time resolution, and the NICER and Swift/XRT light curves have 10 s time resolution. We note that we combined the counts of all three IXPE detectors. During epoch 1, the source flux does not show strong long-timescale variability. NuSTAR and Swift/XRT observed just at the beginning of the first IXPE epoch, whereas NICER overlaps with almost the whole IXPE exposure. During the second epoch, we note that the final flux

has decreased by roughly 10% of its initial value. NuSTAR observed at the end of the IXPE observation together with one of the two Swift/XRT observations.

A.1. All the Observations

IXPE observed GX 339-4 twice during 2024. Swift/XRT, NuSTAR, and NICER observed the source simultaneously to the IXPE epochs. The exact dates of the observations that we considered are reported in Table 2. The NICER Guest Observer program 7702010xxx was also used to monitor the source daily from 2024 January 31 to 2024 February 21. Table 2 shows all the NICER observations of our campaign. When an observation is reported with 0 s exposure, it means that it was performed in orbit day. Due to the optical light leak that is affecting the NICER instruments, these observations cannot be used for scientific analysis. The monitoring of the source started on 2024 January 31, with an almost daily cadence until 2024 February 21. In particular, ObsIDs 7702010111, 7702010112, and 7702010113 are the observations simultaneous to IXPE epoch 1. The monitoring then resumed on 2024 March 8. These last three observations are simultaneous to IXPE epoch 2, but they turned out to be heavily corrupted by the light leak.

A.2. FORS2 Analysis

VLT/FORS2 observed GX 339-4 on three nights during the 2023-2024 outburst, 2024 February 15, March 2, and March 16, as part of a larger optical polarization campaign on the source (M. C. Baglio et al. 2024, in preparation). We consider the first observation, which is simultaneous to IXPE epoch 1, and the last two observations, which are the closest to IXPE epoch 2. Aperture photometry was conducted with the DAOPHOT tool (P. B. Stetson 1987), using a 6 pixel aperture. The normalized Stokes parameters Q and U for linear polarization were calculated following the methods outlined by M. C. Baglio et al. (2020) (Equations (1) and (2)). We note that these parameters are not corrected for instrumental contributions to the linear polarization. However, unpolarized standard stars are regularly observed with FORS2 to monitor the level of instrumental polarization, which has remained stable over the past 10 yr across all bands at a very low level (<0.3%). We then used the algorithm described in M. C. Baglio et al. (2020) and references therein to evaluate the linear polarization of GX 339-4 starting from the parameter $S(\Phi)$ for each HWP angle, defined as

$$S(\Phi) = \left(\frac{f^o(\Phi)/f^e(\Phi)}{f_u^o(\Phi)/f_u^e(\Phi)} - 1\right) / \left(\frac{f^o(\Phi)/f^e(\Phi)}{f_u^o(\Phi)/f_u^e(\Phi)} + 1\right), \quad (A1)$$

where $f^o(\Phi)$ and $f^e(\Phi)$ are the ordinary and extraordinary fluxes of GX 339–4, respectively, and $f_u^o(\Phi)$ and $f_u^e(\Phi)$ are the same quantities calculated for an unpolarized standard star in the field. This parameter is linked to the polarization P of the target and its polarization angle θ by the following equation:

$$S(\Phi) = P\cos 2(\theta - \Phi). \tag{A2}$$

Therefore, a fit of the S parameter with Equation (A2) will give an estimate of the linear P and θ for the target. To increase the significance of the fit, we considered 10 reference field stars in each epoch. Under the simple hypothesis that the field stars are intrinsically unpolarized, this method gives as a result a linear polarization for the target that is already corrected for the

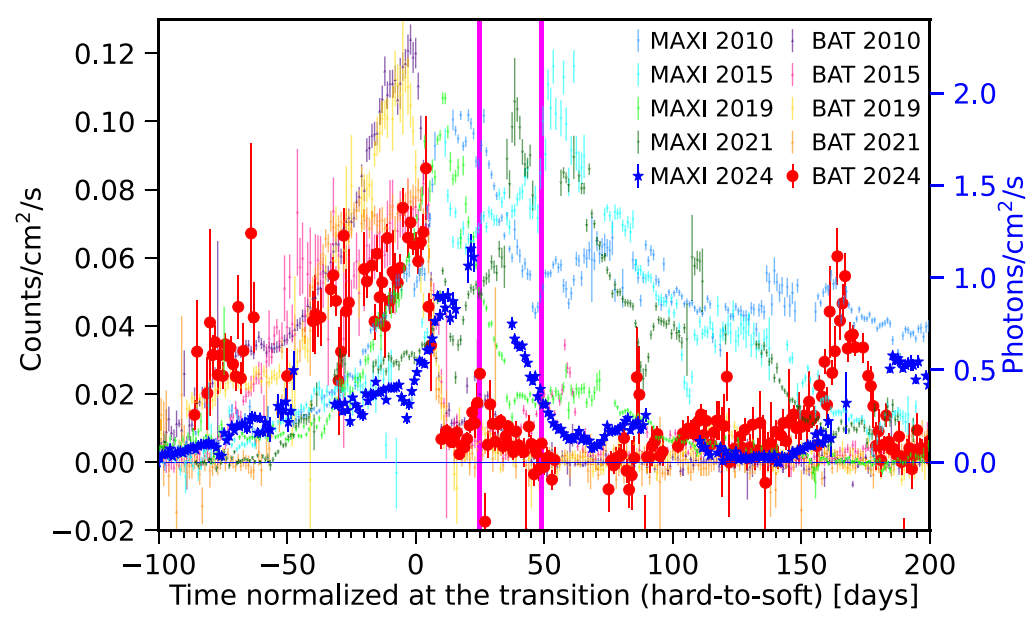


Figure 5. MAXI and Swift/BAT light curves of GX 339–4 outbursts of 2010, 2015, 2019, 2021, and 2024. All the outbursts are synchronized at the beginning of the state transition (day 0). The vertical magenta lines indicate the two epochs discussed in this work for the 2024 outburst (2024 February 14 and 2024 March 8).

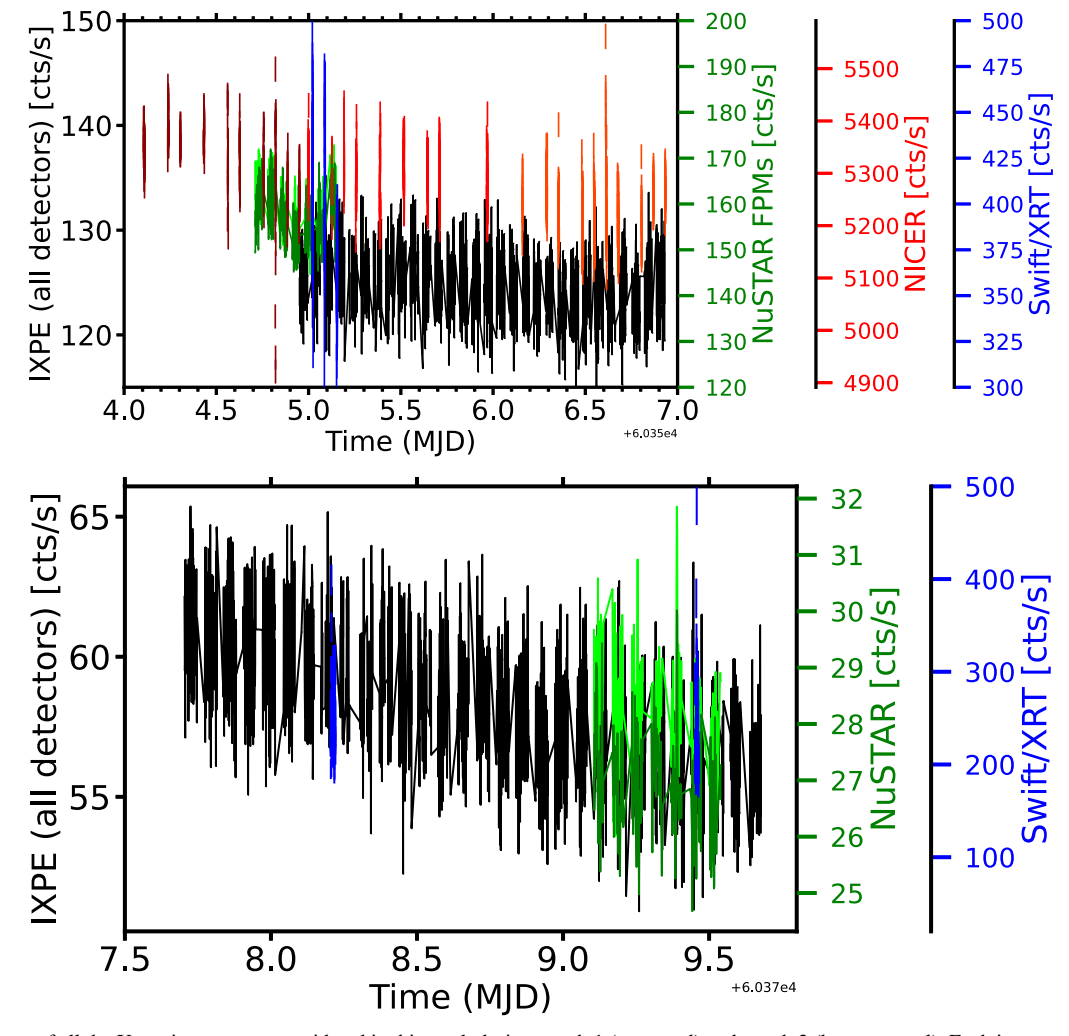


Figure 6. Light curves of all the X-ray instruments considered in this work during epoch 1 (top panel) and epoch 2 (bottom panel). Each instrument has its own y-axis showing the count rate. IXPE (black points) is on the left, while the indicators of the count rate for all the other instruments are on the right (NuSTAR FPMA and FPMB in light and dark green, respectively; Swift/XRT in blue; and NICER in red).

Table 2
The Dates of the Observations by IXPE, Swift/XRT, NuSTAR, NICER, ATCA, and FORS2 Used in This Work

Telescope	ObsID	Start (UT)	End (UT)	Exposure (s)
IXPE (epoch 1)	03005101	2024 Feb 14 22:48:57	2024 Feb 16 22:19:34	94,600
IXPE (epoch 2)	03005301	2024 Mar 08 16:53:26	2024 Mar 10 16:16:18	97,700
Swift/XRT (epoch 1)	00014052207	2024 Feb 15 00:25:11	2024 Feb 15 00:31:56	404
Swift/XRT (epoch 1)	00014052208	2024 Feb 15 02:00:20	2024 Feb 15 02:06:55	394
Swift/XRT (epoch 1)	00014052209	2024 Feb 15 03:35:11	2024 Feb 15 03:41:55	404
Swift/XRT (epoch 2)	00014052219	2024 Mar 09 04:51:32	2024 Mar 09 05:14:56	1400
Swift/XRT (epoch 2)	00016552003	2024 Mar 10 10:47:44	2024 Mar 10 11:04:56	1028
NuSTAR (epoch 1)	91002306002	2024 Feb 14 16:51:09	2024 Feb 15 04:01:09	16,400
NuSTAR (epoch 2)	80902342002	2024 Mar 10 02:31:09	2024 Mar 10 13:21:09	19,500
NICER	7702010101	2024 Jan 31 16:04:28	2024 Jan 31 16:13:13	525
	7702010102	2024 Feb 01 07:34:25	2024 Feb 01 10:48:17	1438
	7702010104	2024 Feb 07 13:44:26	2024 Feb 07 13:52:40	490
	7702010105	2024 Feb 08 05:16:24	2024 Feb 08 22:30:11	3730
	7702010106	2024 Feb 08 23:55:03	2024 Feb 09 18:40:40	1679
	7702010107	2024 Feb 10 07:01:06	2024 Feb 10 14:51:53	636
	7702010108	2024 Feb 11 01:41:39	2024 Feb 11 20:22:13	954
	7702010109	2024 Feb 12 04:04:33	2024 Feb 12 04:07:58	205
	7702010110	2024 Feb 13 14:04:21	2024 Feb 13 20:28:19	986
(epoch 1)	7702010111	2024 Feb 14 02:30:27	2024 Feb 14 22:49:57	3465
(epoch 1)	7702010112	2024 Feb 14 23:55:27	2024 Feb 15 23:17:40	3802
(epoch 1)	7702010113	2024 Feb 16 03:46:45	2024 Feb 16 22:26:00	4778
	7702010114	2024 Feb 17 12:17:23	2024 Feb 17 13:56:00	601
	7702010115	2024 Feb 18 13:03:25	2024 Feb 18 13:12:23	538
	7702010116	2024 Feb 19 15:25:03	2024 Feb 19 15:35:40	635
	7702010117	2024 Feb 20 14:43:29	2024 Feb 20 16:22:00	660
	7702010118	2024 Feb 21 00:03:53	2024 Feb 21 01:39:20	261
(epoch 2)	7702010119	2024 Mar 08 13:02:44	2024 Mar 08 13:02:44	0
(epoch 2)	7702010120	2024 Mar 08 23:54:45	2024 Mar 08 23:54:45	0
(epoch 2)	7702010121	2024 Mar 10 00:40:51	2024 Mar 10 00:40:51	0
ATCA	C3362	2024 May 01 16:30:00	2024 May 01 23:13:00	26,400
FORS2 (epoch 1)	112.25UU.001	2024 Feb 15 08:40:45	2024 Feb 15 09:08:03	1638
	112.25UU.001	2024 Mar 02 06:18:21	2024 Mar 02 06:46:01	1660
	112.25UU.001	2024 Mar 16 09:03:20	2024 Mar 16 09:29:48	1588

low instrumental effects. In addition, if the Q and U Stokes parameters of the reference stars are consistent with each other, this method should, in principle, automatically correct for interstellar polarization along the line of sight. Unfortunately, GX 339-4 is in a highly absorbed region ($A_V = 3.58$ mag, where A_V is the absorption coefficient in the V band; I. A. Kosenkov et al. 2020), and the distance of the source is likely high (10 \pm 2 kpc; A. A. Zdziarski et al. 2019); therefore, it is possible that, despite the correction, some residual interstellar polarization is still present in our results. We note, however, that the interstellar polarization in the direction of GX 339-4 has been estimated in the past by D. M. Russell & R. P. Fender (2008) thanks to polarimetric observations of the source performed close to quiescence. The polarization angle of interstellar dust polarization was estimated to be $\sim 30^{\circ}$; this is not consistent with the (interstellar-dust-subtracted) polarization angle measured in this work, which is instead parallel to the jet axis of GX 339–4. It is therefore unlikely that the optical linear polarization reported in this work has a dominant interstellar origin.

Following M. C. Baglio et al. (2020), to evaluate P and θ , we maximized the Gaussian likelihood function using an optimization algorithm (e.g., the Nelder–Mead algorithm; F. Gao & L. Han 2012) and integrated the posterior probability density of our model parameters using a Markov Chain Monte Carlo algorithm

(D. W. Hogg & D. Foreman-Mackey 2018) based on the "affineinvariant Hamiltonia" algorithm (D. Foreman-Mackey et al. 2013). The chains were initiated from small Gaussian distributions centered on the best-fit values. We discarded the first third of each chain as the "burn-in phase" and ensured that a stationary distribution was reached (S. Sharma 2017). The quality of the fit was assessed as described in L. B. Lucy (2016). The values for Pand θ , along with their 1σ uncertainties, correspond to the 0.16, 0.50, and 0.84 quantiles of the posterior distribution of the parameters. In the case of nondetections, the 99.97th percentile of the posterior distribution of the parameter P was used to estimate an upper limit. The value of θ derived using this method was further adjusted based on observations of the polarized standard star Vela 1-95, with known and documented polarization angles in all FORS2 bands. The average correction applied was negligible, remaining under 2° across all bands and epochs.

Appendix B Spectropolarimetric Fit in Detail

We simultaneously fit the energy spectra of the three Swift/XRT observations and the NuSTAR observation in epoch 1 with the second Swift/XRT observation and the NuSTAR observation in epoch 2. We did not use the NICER spectra since we could use them only for epoch 1 (see Section 2).

Table 3
Parameters of the Fits

		Spectral	Fit: Swift/XRT and I	NuSTAR		
Component	Parameter	Epoch 1 and 2		Component	Parameter	Only Epoch 1
tbnew_feo	$nH (10^{22} cm^{-2})$	$0.4_{-0.1}^{+0.1}$ $2.2_{-0.8}^{+0.8}$ $1.3_{-0.4}^{+0.4}$		tbnew	nH (10 ²² cm ⁻²)	$0.56^{+0.03}_{-0.02}$
	O Fe				, ,	
kerrbb	a incl (deg)	$0.85^{+0.01}_{-0.01} \\ 30^{+2}_{\rm a}$				
		Epoch 1	Epoch 2			Only epoch 1
kerrbb	Mdd (10 ¹⁸ g s ⁻¹) norm	$1.06_{-0.04}^{+0.13} \\ 1.7_{-0.1}^{+0.2}$	$0.6_{-0.2}^{+0.5} \\ 1.9_{-0.2}^{+0.2}$	diskbb	$T_{ m in}$ norm	$0.73_{-0.01}^{+0.01} \\ 3160_{-267}^{+250}$
thcomp	Γ kT _e (keV) cov_frac	$2.35_{-0.02}^{+0.05} \\ 30_{-8}^{+6} \\ 0.17_{-0.01}^{+0.02}$	$2.12^{+0.03}_{-0.03} 797^{b} 0.029^{+0.002}_{-0.014}$	nthcomp	Γ kT _e (keV) norm	$2.39_{-0.04}^{+0.04} \\ 36_{-13}^{+24} \\ 0.85_{-0.05}^{+0.02}$
relline	lineE (keV) Index1 norm	$\begin{array}{c} 6.84^{+0.03}_{-0.06} \\ 4.48^{+0.04}_{-0.13} \\ 0.022^{+0.001}_{-0.003} \end{array}$	$6.71^{+0.06}_{-0.07} \\ 3.3^{+0.3}_{-0.6} \\ 0.002^{+0.001}_{-0.001}$	relline	lineE (keV) Index1 norm	$7.1_{-0.2}^{+0.1} 4.9_{-0.3}^{+0.2} 0.067_{-0.017}^{+0.005}$
smedge	edgeE (keV) MaxTau width (keV)	$7.76_{-0.07}^{+0.04}$ 8_{-3}^{+1} 39_{-10}^{+6}	$7.8_{-0.1}^{+0.1} 2.8^{\circ} 8_{-3}^{+6}$	smedge	edgeE (keV) MaxTau width (keV)	$8.0_{-0.3}^{+0.1} \\ 3_{-1}^{+5} \\ 15_{-6}^{+8}$
Swift Obs2	cal const	$1.00^{+0.01}_{-0.01}$		Swift Obs2	cal const	$1.00^{+0.01}_{-0.01}$
Swift Obs3	cal const	$0.98^{+0.01}_{-0.01}$		Swift Obs3	cal const	$0.98^{+0.01}_{-0.01}$
gain fit—Swift	slope offset (eV)	$1.06_{-0.01}^{+0.01} \\ -84_{-10}^{+11}$	$1.058^{+0.010}_{-0.004} \\ -139^{+12}_{-12}$	gain fit—Swift	slope offset (eV)	$1.059_{-0.007}^{+0.006} \\ -75_{-14}^{+17}$
NuSTAR FPMA	cal const	$0.91^{+0.01}_{-0.01}$	$0.75^{+0.02}_{-0.01}$	NuSTAR FPMA	cal const	$0.90^{+0.02}_{-0.02}$
NuSTAR FPMB	cal const $\chi^2/\text{d.o.f.}$	$0.90^{+0.01}_{-0.02} \\ 2461$	0.73 ^{+0.02} _{-0.01} / 2254	NuSTAR FPMB	cal const $\chi^2/\text{d.o.f.}$	$0.90^{+0.02}_{-0.02}$ $1756/1618$

Notes. On the left: best-fit parameters of the joint fit between the first and the second epochs. The model is constant *TBnew_feo* (thcomp*kerrbb + relline) *smedge, and we fix eta = 0.0, hd = 1.7 in kerrbb. On the right: best-fit parameters of only epoch 1 with the model constant *TBnew* (diskbb + nthcomp + relline) *smedge. We fix inp_type = 1, and we tie kT_bb to $T_{\rm in}$. In both fits, Index2 = 3.0, Rbr = 15 $R_{\rm g}$, inner radius = ISCO, outer radius = 400 $R_{\rm g}$ in relline, and index = -2.67 in smedge. The errors are at the 90% confidence level.

However, we performed some preliminary analysis fitting combinations of the NICER and NuSTAR data and the Swift/XRT and NuSTAR data: all these preliminary fits of epoch 1 were extremely similar. Our best-fit model is TBnew_feo (thcomp*kerrbb + relline)*smedge. All the absorption parameters, the spin of the black hole, and the inclination of the system are tied between the two epochs. Regarding kerrbb, we choose a standard Keplerian disk with zero torque at the inner boundary (eta = 0.0). We also fix the spectral hardening (hd) to 1.7 (T. Shimura & F. Takahara 1995), the distance to 10 kpc, and the black hole mass to $10\,M_\odot$. We include limb darkening, and we do not include self-irradiation in the disk calculation of the kerrbb (rflag = 1 and lflag = 0). All the other parameters are kept free to vary; however, only the mass accretion rate and the normalization vary between the

two epochs in kerrbb. We use the thcomp convolution model to fit the Comptonization component in the spectrum; all its parameters are free to vary between the two epochs since the corona is supposed to change in different states. The only exception is the cosmological redshift, which is set to 0. The relline model is used to fit the iron $K\alpha$ line. Since most of the advanced reflection models (such as the relxill suite of models) do not include self-irradiation from the accretion disk, which should be relevant when the source is in the SIMS and in the soft state, we decided not to use them.

We fit the Swift/XRT spectra with a gain shift (xspec command gain fit). We allow both slope and offset to vary during the fit; however, we tie these two parameters between the three Swift/XRT observations of epoch 1. Using a gain shift is suggested by the International Astronomical

^a The lower limit of the inclination is 30.

^b The electron temperature of epoch 2 is not constrained (fit range 0.5-900 keV).

^c The MaxTau value is not constrained (fit range 0–5).

d The systematics are not accounted for by the Cash statistic; thus, the statistical errors quoted are unrealistically small.

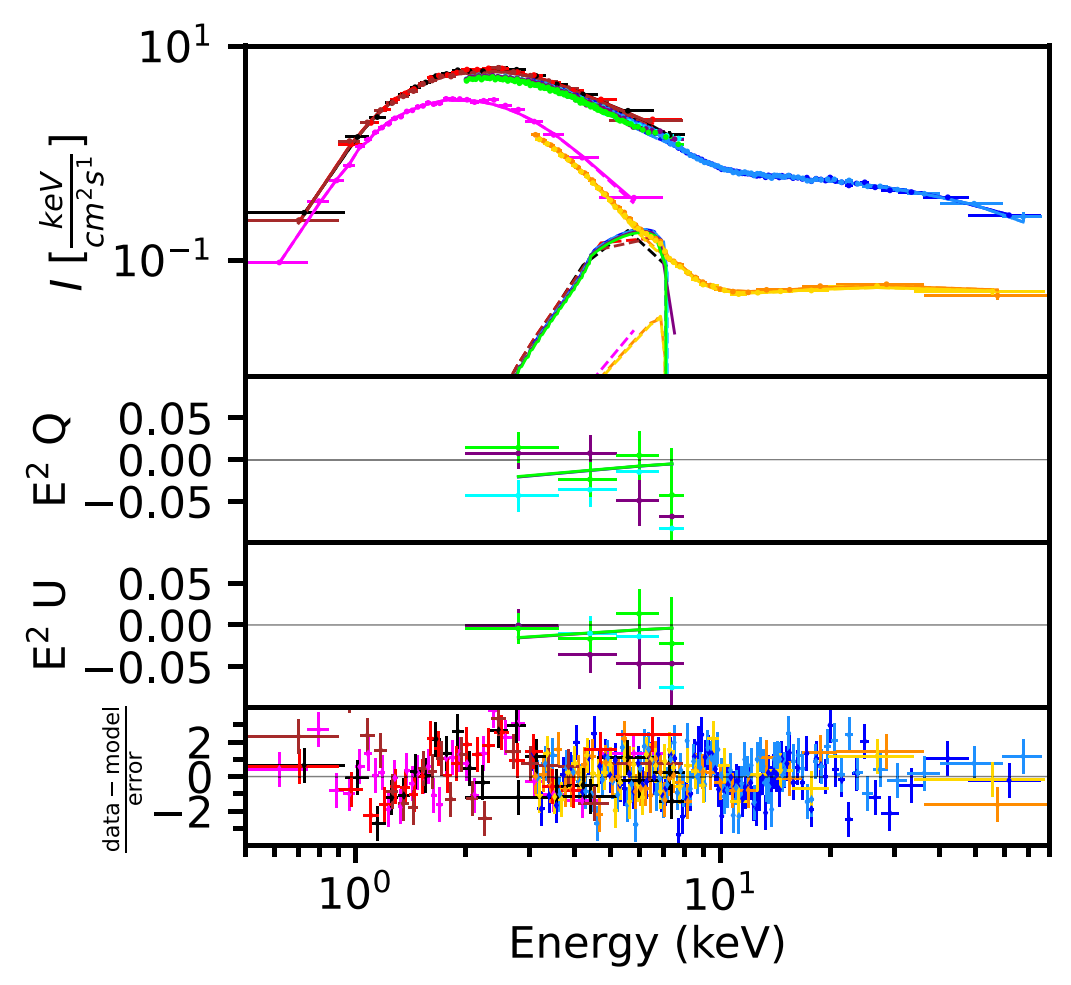


Figure 7. Top: unfolded spectra of the two epochs. Spectra of epoch 1: Swift/XRT (black, red, and brown), NuSTAR FPMA and FPMB (dark blue and light blue), and three IXPE detectors (light green, purple, and cyan). Spectra of epoch 2: Swift/XRT (magenta) and NuSTAR FPMA and FPMB (yellow and orange). Central panels: energy spectrum of Stokes parameters Q and U of epoch 1 only (the colors match the flux-energy spectrum). Bottom: spectral fit residuals of only Swift/XRT and NuSTAR spectra for both epochs (the colors match the flux-energy spectrum).

 Table 4

 Spectropolarimetric Calibration Constants

Calibration Parameters for Spectropolarimetric Fit ^a					
	Parameter	Epoch 1 (3–8 keV)	Epoch 2 (2–8 keV)		
	P_{X}	$1.3 \pm 0.3\% \ (1\sigma)$	<1.2% (3\sigma)		
	θ_{X}	$-74^{\circ} \pm 7^{\circ} (1\sigma)$	•••		
IXPE det1	cal const	$0.876^{+0.004}_{-0.004}$	$0.793^{+0.007}_{-0.006}$		
gain fit	slope	$0.967^{+0.002}_{-0.002}$	$0.984^{+0.003}_{-0.003}$		
	offset (eV)	30^{+7}_{-7}	7^{+12}_{-11}		
IXPE det2	cal const	$0.873^{+0.004}_{-0.004}$	$0.794^{+0.007}_{-0.007}$		
gain fit	slope	$0.975^{+0.002}_{-0.002}$	$0.965^{+0.003}_{-0.003}$		
	offset (eV)	28^{+8}_{-7}	52^{+12}_{-13}		
IXPE det3	cal const	$0.848^{+0.004}_{-0.004}$	$0.760^{+0.007}_{-0.007}$		
gain fit	slope	$0.972^{+0.002}_{-0.002}$	$0.982^{+0.003}_{-0.003}$		
	offset (eV)	28^{+7}_{-8}	23^{+12}_{-12}		
	$\chi^2/\text{d.o.f.}$	3871/3611	3799/3611		

Note. The errors are at the 90% confidence level apart from P_X and θ_X , which are specified in the table.

Consortium for High-Energy Calibration. In particular, K. K. Madsen et al. (2017) reported that Swift/XRT high signal-to-noise spectra of bright sources occasionally show

residuals of the 10% level, suggesting the use of the gain command in xspec to mitigate this effect. We note that the fit requires higher values of the gain offset, 84 \pm 20 eV for epoch 1 and 140 \pm 20 eV³⁷ compared to what is suggested by K. K. Madsen et al. (2017; $\sim\pm10$ to 50 eV). Table 3 shows the best-fit parameter values. The reduced χ^2 is 2461 over 2254 degrees of freedom (d.o.f.). Figure 7 shows the unfolded spectra of the two epochs: black, red, and brown symbols are the three Swift/XRT energy spectra of epoch 1; dark blue and light blue are the FPMA and FPMB NuSTAR spectra of epoch 1; magenta is the Swift/XRT spectrum of epoch 2; and yellow and orange are the FPMA and FPMB NuSTAR spectra of epoch 2. The residuals match the colors of the spectra. We note that the residuals show a few features around low energies (below 3 keV); this might be due to possible instrumental features that have been reported by the calibration team³⁸ due to the high-energy proton interactions causing damage to the CCD.³⁹

After we establish the best fit, we add the IXPE spectra I, Q, and U for each of the three IXPE detectors, allowing us to measure the polarization of the source. We freeze all the

^a All the previous parameters are fixed apart from calibration constants and gain fit parameters.

 $[\]overline{^{37}}$ Errors are quoted at 3σ .

 $^{^{38}}$ https://heasarc.gsfc.nasa.gov/docs/heasarc/caldb/swift/docs/xrt/SWIFT-XRT-CALDB-09_v19.pdf

³⁹ For example, near the Au–M V edge at 2.205 keV, the Si–K edge at 1.839 keV, or the O–K edge at 0.545 keV (see K. K. Madsen et al. 2017).

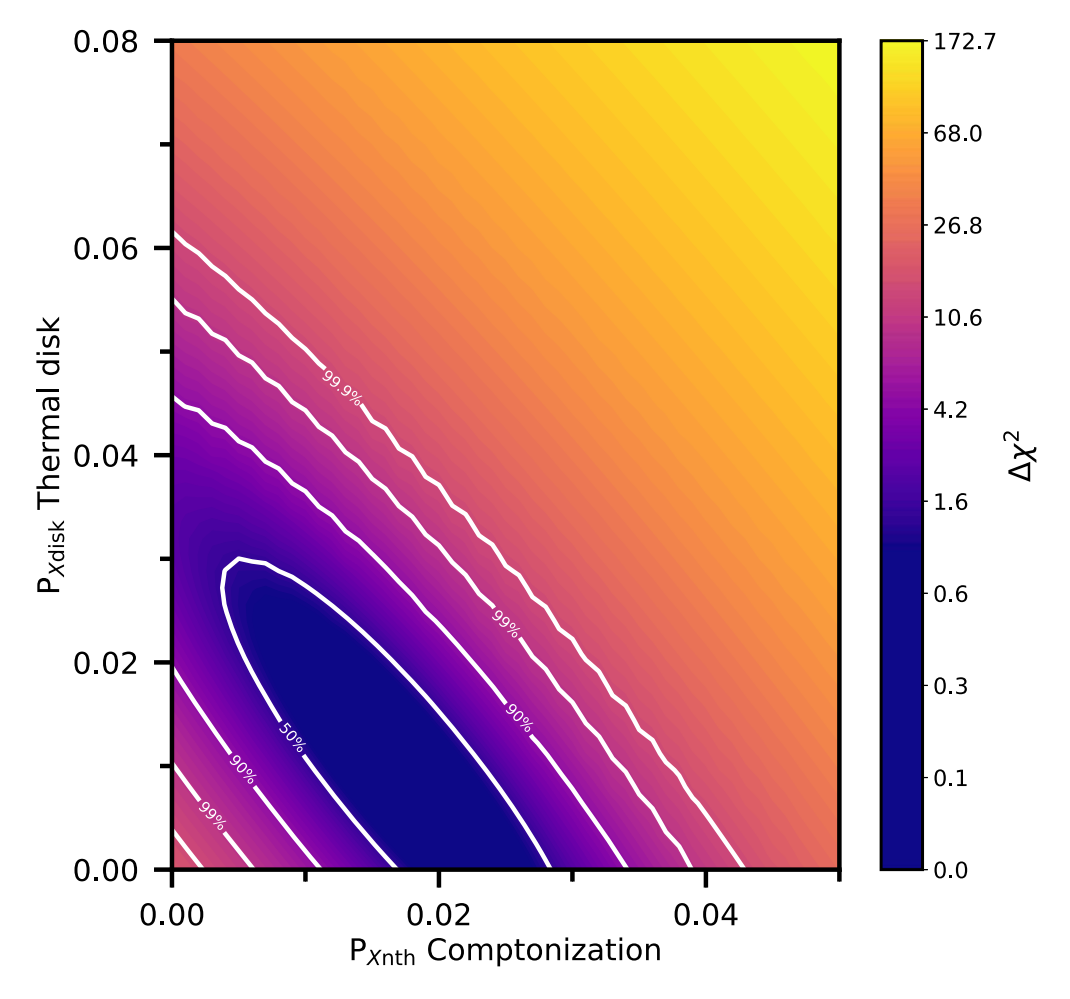


Figure 8. Epoch 1 contour plot of the disk component polarization fraction $P_{X,disk}$ vs. the Comptonization component polarization fraction $P_{X,nth}$, when the θ_X values of the two components are forced to be aligned. Best-fit parameter values of the full model are reported on the right side of Table 3. The IXPE data are restricted to the 3–8 keV energy range.

physical parameters to the best-fit values and leave the calibration constants free to vary among all the instruments. We note that the gain fit functionality of xspec is required to fit the energy spectra of the three IXPE detectors. Figure 7 shows the three IXPE I spectra of epoch 1 in the top panel (light green, purple, and cyan for detectors 1, 2, and 3, respectively) and the Q and U spectra of each detector in the middle panels (matching the colors of the I spectra). We apply the polconst multiplicative model to the entire spectral model. As we explained in the main text, we measure significant P only when we consider the 3-8 keV band of the IXPE Stokes parameter energy spectra. We analyzed IXPE epoch 2 with the exact same procedure. In Table 4, we report the polarization best-fit values of $P_{\rm X}$ and $\theta_{\rm X}$, along with the values of the calibration constants, the gain curve, and the pointing offset corrections in the 3-8 keV energy band for epoch 1 and the full IXPE energy band (2-8 keV) for epoch 2.

In order to allow the spectral components to have different polarization values, we cannot use the convolution model thcomp. Therefore, even though we lose self-consistency, we fit only epoch 1 with the model TBnew*(diskbb + nthcomp + relline)*smedge. We use TBnew instead of TBnew_feo because it is unnecessary to allow oxygen and iron abundances to vary to fit just epoch 1. We follow the same procedure as in the previous case,

finding the best fit without IXPE spectra and freezing the values of the parameters apart from the calibration constants among the instruments. Table 3 shows the best-fit values and the reduced χ^2 , which indicates that we obtain an acceptable fit. We then multiply each of the additive components of the model by polconst and fix the $P_{\rm X}$ of the iron line to zero because reflection lines are not supposed to be polarized (F. Podgorný et al. 2022). We test this model configuration only considering the IXPE data in the energy range where we detected polarization, i.e., 3–8 keV. We first fit allowing either the disk component or the Comptonization component to be polarized. In the first case, the polarization of the disk component is $P_{\rm X,disk} = 2.0\% \pm 0.5\%$ and $\theta_{\rm X,disk} = -75^{\circ} \pm 7^{\circ}$, while in the second case, the polarization of the Comptonization component is $P_{\rm X,nth} = 3.6\% \pm 0.1\%$ and $\theta_{\rm X,nth} = -73^{\circ} \pm 7^{\circ}$ (1σ errors).

Finally, we test two scenarios. First, we allow the $P_{\rm X}$ of both components to be free, and we tie the $\theta_{\rm X,disk}$ and $\theta_{\rm X,nth}$ to be the same; second, we force the $\theta_{\rm X,disk}$ to be 90° off from the $\theta_{\rm X,nth}$ value, which is free to vary in the fit. Figures 8 and 9 show the contour plots of the two $P_{\rm X}$ components in the first and second tests, respectively. It is interesting to note that, when the polarization angles are forced to be perpendicular, only one component can have a strong polarization degree, further strengthening the conclusion that the polarization angle can only be $\sim -74^\circ$.

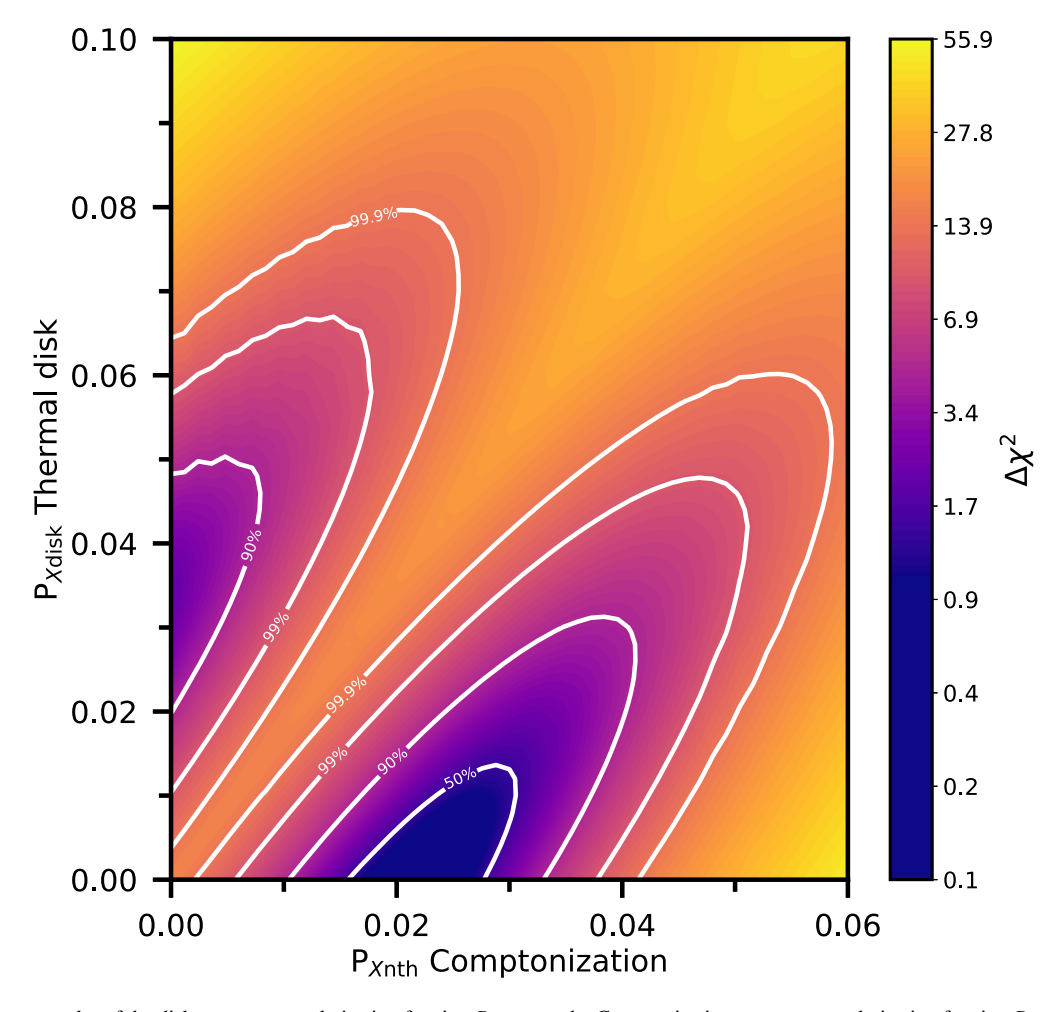


Figure 9. Epoch 1 contour plot of the disk component polarization fraction $P_{X,\text{disk}}$ vs. the Comptonization component polarization fraction $P_{X,\text{nth}}$, when the θ_X values of the two components are forced to be perpendicular to each other. Best-fit parameter values of the full model are reported on the right side of Table 3. The IXPE data are restricted to the 3–8 keV energy range.

ORCID iDs

G. Mastroserio https://orcid.org/0000-0003-4216-7936 B. De Marco https://orcid.org/0000-0003-2743-6632 M. C. Baglio https://orcid.org/0000-0003-1285-4057 F. Carotenuto https://orcid.org/0000-0002-0426-3276 S. Fabiani https://orcid.org/0000-0003-1533-0283 T. D. Russell https://orcid.org/0000-0002-7930-2276 F. Capitanio https://orcid.org/0000-0002-6384-3027 Y. Cavecchi https://orcid.org/0000-0002-6447-3603 D. M. Russell https://orcid.org/0000-0002-3500-631X M. Dovčiak https://orcid.org/0000-0003-0079-1239 M. Del Santo https://orcid.org/0000-0002-1793-1050 K. Alabarta https://orcid.org/0000-0003-0168-9906 A. Ambrifi https://orcid.org/0000-0003-1536-4213 S. Campana https://orcid.org/0000-0001-6278-1576 P. Casella https://orcid.org/0000-0002-0752-3301 S. Covino https://orcid.org/0000-0001-9078-5507 G. Illiano https://orcid.org/0000-0003-4795-7072 E. Kara https://orcid.org/0000-0003-0172-0854 E. V. Lai https://orcid.org/0000-0002-6421-2198 G. Lodato https://orcid.org/0000-0002-2357-7692 A. Marino https://orcid.org/0000-0001-5674-4664 P. Saikia https://orcid.org/0000-0002-5319-6620 A. W. Shaw https://orcid.org/0000-0002-8808-520X

J. Svoboda https://orcid.org/0000-0003-2931-0742
 F. M. Vincentelli https://orcid.org/0000-0002-1481-1870
 J. Wang https://orcid.org/0000-0002-1742-2125

References

Alabarta, K., Altamirano, D., Méndez, M., et al. 2021, MNRAS, 507, 5507 Alabarta, K., Baglio, M. C., Russell, D. M., et al. 2024, ATel, 16460, 1 Alabarta, K., Homan, J., Russell, D. M., et al. 2023, ATel, 16260, 1 Bachetti, M., & Huppenkothen, D. 2018, ApJL, 853, L21 Bachetti, M., Huppenkothen, D., Khan, U., et al. 2024, StingraySoftware/ stingray: Release 2.1, v2.1, Zenodo, doi:10.5281/zenodo.11383212 Baglio, M. C., D'Avanzo, P., Campana, S., et al. 2016, A&A, 591, A101 Baglio, M. C., Russell, D. M., Crespi, S., et al. 2020, ApJ, 905, 87 Baldini, L., Bucciantini, N., Lalla, N. D., et al. 2022, SoftX, 19, 101194 Barthelmy, S. D., Barbier, L. M., Cummings, J. R., et al. 2005, SS Belloni, T., Homan, J., Casella, P., et al. 2005, A&A, 440, 207 Belloni, T. M. 2010, in Lecture Notes in Physics, ed. T. Belloni, Vol. 794 (Berlin: Springer), 53 Belloni, T. M., Zhang, L., Kylafis, N. D., Reig, P., & Altamirano, D. 2020, MNRAS, 496, 4366 Briggs, D. S. 1995, PhD thesis, New Mexico Institute of Mining and Technology Bright, J. S., Fender, R. P., Motta, S. E., et al. 2020, NatAs, 4, 697 Brown, J. C., McLean, I. S., & Emslie, A. G. 1978, A&A, 68, 415 Burrows, D. N., Hill, J. E., Nousek, J. A., et al. 2005, SSRv, 120, 165 Cadolle Bel, M., Rodriguez, J., D'Avanzo, P., et al. 2011, A&A, 534, A119 Carotenuto, F., Corbel, S., Tremou, E., et al. 2021, MNRAS, 504, 444

```
CASA Team, Bean, B., Bhatnagar, S., et al. 2022, PASP, 134, 114501
Casella, P., Belloni, T., & Stella, L. 2005, ApJ, 629, 403
Chandrasekhar, S. 1960, PNAS, 46, 253
Connors, R. M. T., van Eijnatten, D., Markoff, S., et al. 2019, MNRAS,
  485, 3696
Connors, R. M. T., Garcia, J. A., Tomsick, J., et al. 2021, ApJ, 909, 146
Corbel, S., Aussel, H., Broderick, J. W., et al. 2013, MNRAS, 431, L107
Corbel, S., Fender, R. P., Tzioumis, A. K., et al. 2002, Sci, 298, 196
Coriat, M., Corbel, S., Buxton, M. M., et al. 2009, MNRAS, 400, 123
Dauser, T., Garcia, J., Parker, M. L., Fabian, A. C., & Wilms, J. 2014,
         AS, 444, L100
De Marco, B., Ponti, G., Muñoz-Darias, T., & Nandra, K. 2015, ApJ, 814, 50
De Marco, B., Ponti, G., Petrucci, P. O., et al. 2017, MNRAS, 471, 1475
De Marco, B., Zdziarski, A. A., Ponti, G., et al. 2021, A&A, 654, A14
Dexter, J., & Begelman, M. C. 2024, MNRAS, 528, L157
Di Marco, A., Costa, E., Muleri, F., et al. 2022, AJ, 163, 170
Di Marco, A., Soffitta, P., Costa, E., et al. 2023, AJ, 165, 143
Dolan, J. F. 1984, A&A, 138, 1
Dolan, J. F., & Tapia, S. 1989, PASP, 101, 1135
Done, C., Gierliński, M., & Kubota, A. 2007, A&ARv, 15, 1
Dovčiak, M., Muleri, F., Goosmann, R. W., Karas, V., & Matt, G. 2008,
   MNRAS, 391, 32
Fabian, A. C., Rees, M. J., Stella, L., & White, N. E. 1989, MNRAS, 238, 729
Fender, R. P., Belloni, T. M., & Gallo, E. 2004, MNRAS, 355, 1105
Fender, R. P., Homan, J., & Belloni, T. M. 2009, MNRAS, 396, 1370
Foreman-Mackey, D., Hogg, D. W., Lang, D., & Goodman, J. 2013, PASP,
Gallo, E., Corbel, S., Fender, R. P., Maccarone, T. J., & Tzioumis, A. K. 2004,
   MNRAS, 347, L52
Gandhi, P., Blain, A. W., Russell, D. M., et al. 2011, ApJL, 740, L13
Gao, F., & Han, L. 2012, Comp. Opt. and Appl., 51, 259
Garcia, F., Méndez, M., Karpouzas, K., et al. 2021, MNRAS, 501, 3173
Garcia, J., Dauser, T., Lohfink, A., et al. 2014, ApJ, 782, 76
Gendreau, K. C., Arzoumanian, Z., Adkins, P. W., et al. 2016, Proc. SPIE,
   9905, 99051H
Gliozzi, M., Bodo, G., Ghisellini, G., Scaltriti, F., & Trussoni, E. 1998, A&A,
  337, L39
Harrison, F. A., Craig, W. W., Christensen, F. E., et al. 2013, ApJ, 770, 103
Heida, M., Jonker, P. G., Torres, M. A. P., & Chiavassa, A. 2017, ApJ,
   846, 132
Hogg, D. W., & Foreman-Mackey, D. 2018, ApJS, 236, 11
Homan, J., Buxton, M., Markoff, S., et al. 2005, ApJ, 624, 295
Homan, J., Wijnands, R., van der Klis, M., et al. 2001, ApJS, 132, 377
Homan, J., Bright, J., Motta, S. E., et al. 2020, ApJL, 891, L29
Huppenkothen, D., Bachetti, M., Stevens, A. L., et al. 2019, ApJ, 881, 39
Ingram, A., Bollemeijer, N., Veledina, A., et al. 2024, ApJ, 968, 76
Ingram, A. R., & Motta, S. E. 2019, NewAR, 85, 101524
Kaastra, J. S., & Bleeker, J. A. M. 2016, A&A, 587, A151
Kosenkov, I. A., Veledina, A., Suleimanov, V. F., & Poutanen, J. 2020, A&A,
   638, A127
Kotov, O., Churazov, E., & Gilfanov, M. 2001, MNRAS, 327, 799
Kravtsov, V., Berdyugin, A. V., Kosenkov, I. A., et al. 2022, MNRAS,
   514, 2479
Krawczynski, H., Muleri, F., Dovčiak, M., et al. 2022, Sci, 378, 650
Lucy, L. B. 2016, A&A, 588, A19
Lyubarskii, Y. E. 1997, MNRAS, 292, 679
Lyutikov, M., Pariev, V. I., & Gabuzda, D. C. 2005, MNRAS, 360, 869
Ma, R., Méndez, M., Garcia, F., et al. 2023, MNRAS, 525, 854
Madsen, K. K., Beardmore, A. P., Forster, K., et al. 2017, AJ, 153, 2
Markert, T. H., Canizares, C. R., Clark, G. W., et al. 1973, ApJL, 184, L67
Markoff, S., Nowak, M. A., & Wilms, J. 2005, ApJ, 635, 1203
Marra, L., Brigitte, M., Rodriguez Cavero, N., et al. 2024, A&A, 684, A95
Mastroserio, G., Ingram, A., & van der Klis, M. 2018, MNRAS, 475, 4027
Mastroserio, G., Ingram, A., Wang, J., et al. 2021, MNRAS, 507, 55
Matsuoka, M., Kawasaki, K., Ueno, S., et al. 2009, PASJ, 61, 999
Miller-Jones, J. C. A., Sivakoff, G. R., Altamirano, D., et al. 2012, MNRAS,
Miller-Jones, J. C. A., Tetarenko, A. J., Sivakoff, G. R., et al. 2019, Natur,
   569, 374
Mirabel, I. F., & Rodriguez, L. F. 1994, Natur, 371, 46
```

Moscibrodzka, M. A., & Yfantis, A. I. 2023, ApJS, 265, 22

```
Motta, S., Muñoz-Darias, T., Casella, P., Belloni, T., & Homan, J. 2011,
  MNRAS, 418, 2292
Motta, S. E., Casella, P., Henze, M., et al. 2015, MNRAS, 447, 2059
Muñoz-Darias, T., Motta, S., & Belloni, T. M. 2011, MNRAS, 410, 679
Negoro, H., Kudo, Y., Nakajima, M., et al. 2024, ATel, 16598, 1
Negoro, H., Nakajima, M., Kobayashi, K., et al. 2023, ATel, 16302, 1
Nespoli, E., Belloni, T., Homan, J., et al. 2003, A&A, 412, 235
Novikov, I. D., & Thorne, K. S. 1973, in Black Holes, ed. C. DeWitt &
  B. DeWitt (New York: Gordon and Breach), 343
Nowak, M. A., Wilms, J., Heinz, S., et al. 2005, ApJ, 626, 1006
Nyamai, M. M., Tremou, L., Fender, R., & Team, X-K.A.T. 2024, ATel,
  16421, 1
Peirano, V., Méndez, M., Garcia, F., & Belloni, T. 2023, MNRAS, 519, 1336
Plant, D. S., Fender, R. P., Ponti, G., Muñoz-Darias, T., & Coriat, M. 2014,
  MNRAS, 442, 1767
Podgorný, J., Dovčiak, M., Marin, F., Goosmann, R., & Różańska, A. 2022,
   MNRAS, 510, 4723
Podgorný, J., Marra, L., Muleri, F., et al. 2023, MNRAS, 526, 5964
Poutanen, J., & Svensson, R. 1996, ApJ, 470, 249
Poutanen, J., Veledina, A., & Zdziarski, A. A. 2018, A&A, 614, A79
Ratheesh, A., Dovčiak, M., Krawczynski, H., et al. 2024, ApJ, 964, 77
Rodriguez Cavero, N., Marra, L., Krawczynski, H., et al. 2023, ApJL,
  958, L8
Russell, D. M. 2023, AN, 344, e20230017
Russell, D. M., Casella, P., Fender, R. P., et al. 2010, in Proc. of High Time
   Resolution Astrophysics—The Era of Extremely Large Telescopes (HTRA-
   IV) (Trieste: SISSA), 9
Russell, D. M., Casella, P., Kalemci, E., et al. 2020, MNRAS, 495, 182
Russell, D. M., & Fender, R. P. 2008, MNRAS, 387, 713
Russell, D. M., & Shahbaz, T. 2014, MNRAS, 438, 2083
Russell, D. M., Shahbaz, T., Lewis, F., & Gallo, E. 2016, MNRAS, 463, 2680
Russell, T. D., Carotenuto, F., Miller-Jones, J. C. A., et al. 2024, ATel,
  16621, 1
Russell, T. D., Tetarenko, A. J., Miller-Jones, J. C. A., et al. 2019, ApJ,
Russell, T. D., Lucchini, M., Tetarenko, A. J., et al. 2020, MNRAS, 498, 5772
Salvesen, G. 2022, ApJL, 940, L22
Schnittman, J. D., & Krolik, J. H. 2009, ApJ, 701, 1175
Schnittman, J. D., & Krolik, J. H. 2010, ApJ, 712, 908
Shahbaz, T. 2019, in Astronomical Polarization from the Infrared to Gamma
   Rays, ed. R. Mignani et al. (Cham: Springer), 247
Shahbaz, T., Russell, D. M., Covino, S., et al. 2016, MNRAS, 463, 1822
Shakura, N. I., & Sunyaev, R. A. 1973, A&A, 24, 337
Sharma, S. 2017, ARA&A, 55, 213
Shimura, T., & Takahara, F. 1995, ApJ, 445, 780
Sobolev, V. V., & Minin, I. N. 1963, P&SS, 11, 657
Soleri, P., Belloni, T., & Casella, P. 2008, MNRAS, 383, 1089
Steiner, J. F., Nathan, E., Hu, K., et al. 2024, ApJL, 969, L30
Stetson, P. B. 1987, PASP, 99, 191
Svoboda, J., Dovčiak, M., Steiner, J. F., et al. 2024, ApJ, 960, 3
Taverna, R., Marra, L., Bianchi, S., et al. 2021, MNRAS, 501, 3393
Tetarenko, B. E., Sivakoff, G. R., Heinke, C. O., & Gladstone, J. C. 2016,
    ApJS, 222, 15
Thorne, K. S., & Price, R. H. 1975, ApJL, 195, L101
Tingay, S. J., Jauncey, D. L., Preston, R. A., et al. 1995, Natur, 374, 141
Uttley, P., Cackett, E. M., Fabian, A. C., Kara, E., & Wilkins, D. R. 2014,
         v, 22, 72
Uttley, P., & Malzac, J. 2024, MNRAS, Advance Access
Veledina, A. 2018, MNRAS, 481, 4236
Veledina, A., Muleri, F., Dovčiak, M., et al. 2023, ApJL, 958, L16
Wang, J., Kara, E., Lucchini, M., et al. 2022, ApJ, 930, 18
Wang, J., Kara, E., Steiner, J. F., et al. 2020, ApJ, 899, 44
Wang, J., Mastroserio, G., Kara, E., et al. 2021, ApJL, 910, L3
Weisskopf, M. C., Soffitta, P., Baldini, L., et al. 2022, JATIS, 8, 026002
White, N. E., Nagase, F., & Parmar, A. N. 1995, in X-ray Binaries, ed.
   W. H. G. Lewin, J. van Paradijs, & E. P. J. van den Heuvel (Cambridge:
  Cambridge Univ. Press), 1
Wood, C. M., Miller-Jones, J. C. A., Bahramian, A., et al. 2024, ApJL, 971, L9
Wood, C. M., Miller-Jones, J. C. A., Homan, J., et al. 2021, MNRAS,
  505, 3393
Zdziarski, A. A., Ziółkowski, J., & Mikołajewska, J. 2019, MNRAS, 488, 1026
```